Radiogenic isotopic and clay mineralogical signatures of terrigenous particles as water-mass tracers

Beny, F.; Bout-Roumazeilles, V.; Davies, G. R.; Waelbroeck, C.; Bory, A.; Tribovillard, N.; Delattre, M.; Abraham, R.

published in
Quaternary Science Reviews
2020

DOI (link to publisher)
10.1016/j.quascirev.2019.106089

document version
Publisher's PDF, also known as Version of record

Quaternary Science Reviews 228 (2020) 106089

Contents lists available at ScienceDirect

Quaternary Science Reviews

journal homepage: www.elsevier.com/locate/quascirev

Radiogenic isotopic and clay mineralogical signatures of terrigenous particles as water-mass tracers: New insights into South Atlantic deep circulation during the last termination

F. Beny [a, b, *], V. Bout-Roumazeilles [a], G.R. Davies [b], C. Waelbroeck [c], A. Bory [a], N. Tribovillard [a], M. Delattre [a], R. Abraham [a]

[a] Laboratoire d'Océanologie et de Géosciences, UMR 8187 CNRS/Univ Lille/ULCO, Cité scientifique, F-59655, Villeneuve d'Ascq, France
[b] VU University Amsterdam, Department of Earth Sciences, Faculty of Science, De Boelelaan 1085, 1081 HV, Amsterdam, the Netherlands
[c] Laboratoire des Sciences du Climat et de l'Environnement, LSCE/IPSL, UMR 8212 CEA-CNRS-UVSQ, Site de l'Orme des Merisiers, F-91191, Gif sur Yvette Cedex, France

ARTICLE INFO

Article history:
Received 27 June 2019
Received in revised form
1 October 2019
Accepted 17 November 2019
Available online 28 November 2019

Keywords:
Last deglaciation
Paleoceanography
Southern Ocean
South Atlantic
Radiogenic isotopes
Clay mineralogy
Grain size distribution

ABSTRACT

The past evolution of the Southern Ocean, one of the major components of the climatic system, is still a matter of debate. This study provides new insights into the deep Southern Ocean circulation based on the radiogenic isotopes and clay mineralogical signature of the terrigenous fractions transported by the main deep water masses to sediments recovered in core MD07-3076Q from the central South Atlantic. This approach successfully permits: (1) provenance identification of the various grain-size fractions (clay, cohesive silt and sortable silt); (2) assignment of each grain-size fraction to a specific water-mass; (3) reconstruction of past changes in the main deep water-mass pathways. These data document the evolution of deep-water masses in the South Atlantic Ocean during the last deglaciation. The Antarctic Bottom Water (AABW) speed and northward extension were maximum at the end of the Last Glacial Maximum (LGM), associated with strong bottom water production in the Weddell Sea, together with a vigorous Lower Circumpolar Deep Water (LCDW). In contrast the North Atlantic Deep Water (NADW) circulation was weaker than today. The onset of the deglaciation (from 17.5 ka to 15 ka, ~Heinrich Stadial 1, HS 1) was marked by weakening and southerly retreat of the AABW and by an increase of mixing between AABW and LCDW. The speed of the AABW remained at its lowest during the Bølling Allerød (B/A) and the Younger Dryas (YD), and the LCDW slowed and retreated to the south, while the NADW progressively migrated southward, deepened, and strengthened between the beginning of the Bølling Allerød and the Holocene (from ~15 to 10 ka).

1. Introduction

The Southern Ocean (SO) is a key area for understanding the present and past carbon cycle. Direct observations indicate that the SO is a sink of atmospheric CO_2 today (Le Quéré et al., 2007; Sallée et al., 2012) while it was likely a source of CO_2 to the atmosphere during the deglaciation (Bouttes et al., 2012; Jaccard et al., 2013). Upwelling of CO_2-rich deep water likely explains most of the CO_2 rise observed during Heinrich Stadials (HS; Ahn and Brook, 2008; Anderson et al., 2009; Fischer et al., 2010; Skinner et al., 2010; Menviel et al., 2014, 2017). Several other processes occurring in the Southern Ocean have also been invoked to explain the deglacial atmospheric CO_2 rise. For example, reduction of biological pump due to reduced iron fertilization (Watson et al., 2000; Wolff et al., 2006; Fischer et al., 2010; Martínez-García et al., 2014); reduced CO_2 solubility due to increased temperature of the ocean (Köhler and Fischer, 2006; Fischer et al., 2010); reduction of sea ice extent (Fischer et al., 2010). As a consequence, the organization and extension of the Southern Ocean deep water-masses (i.e., Atlantic Meridional Overturning Circulation, AMOC; Skinner et al., 2010; Shakun et al., 2012; Toggweiler et al., 2006) were studied, mainly using paleo-hydrological proxies ($\delta^{18}O$, $\delta^{13}C$, ε_{Nd} of sea water, $\Delta^{13}C$; Barker et al., 2009; Vásquez-Riveiros et al., 2010; Skinner et al., 2010, 2013, 2014; Waelbroeck et al., 2011; Gottschalk et al.,

* Corresponding author. Laboratoire d'Océanologie et de Géosciences, UMR 8187 CNRS/Univ Lille/ULCO, Cité scientifique, F-59655, Villeneuve d'Ascq, France.
E-mail address: beny.francois@gmail.com (F. Beny).

https://doi.org/10.1016/j.quascirev.2019.106089
0277-3791/

2015b). By contrast, the terrigenous particle signal transported by these deep water-masses in the sub-Antarctic Atlantic Ocean remain poorly studied, even though locally it was successfully used to reconstruct the deep ocean circulation dynamical component (Diekmann et al., 2000 – Scotia Sea; Walter et al., 2000 – Scotia Sea and southwest South Atlantic; Kuhn and Diekmann, 2002 – Cape Basin). In this study, we aim to reconstruct the past evolution of deep-water masses (i.e. contribution to sedimentation, vertical and horizontal extensions, and speeds) during the last deglaciation using the signal carried in the terrigenous particles transported by these water masses. Sediment grain size distribution allows identifying the contribution of distinct oceanic currents (Weltje and Prins, 2007; Weltje, 2012), and reconstructing the speeds of the main deep water-masses (McCave and Hall, 2006; McCave and Andrews, 2019). Grain-size distribution displays distinct modes (Weltje, 2012) that can be attributed to specific physical transport processes (e.g., wind, water currents, ice) and/or transport energy. Because grain-size distribution reflects both carrying vectors (e.g., wind, water currents, ice) and flow speed, several studies focused on the respective isotopic composition of distinct grain-size fractions in order to track distinct provenance patterns (Meyer et al., 2011; Bayon et al., 2015; Beny et al., 2018). Similarly, clay minerals are useful tracers of provenance, erosion balance, weathering, and transportation pattern of fine-grained sediments (Moriarty, 1977; Petschick et al., 1996; Kuhn and Diekmann, 2002; Montero-Serrano et al., 2010). Finally, radiogenic isotope compositions of sediments can be used to decipher the different provenances of terrigenous particles and determine their respective contributions through time (Walter et al., 2000; Bayon et al., 2009).

This study focuses on the South Atlantic Ocean, where northern water-masses (North Atlantic Deep Water, NADW) and southern ones (Lower Circumpolar Deep Water, LCDW and Antarctic Bottom Water, AABW) mix, because this area is key for understanding the atmosphere-ocean exchanges that control CO_2 sequestration/outgassing. The reorganization of these deep water-masses during the deglaciation is still a subject of debate and their impact on deglaciation is not resolved (Barker et al., 2009; Skinner et al., 2010, 2013; Waelbroeck et al., 2011; Adkins, 2013; Menviel et al., 2014, 2015a,b, 2018). Recent studies of the last deglaciation ventilation events in the South Atlantic Ocean demonstrated an apparent synergy between physical and biological processes (Gottschalk et al., 2016), whereas chemical and physical processes appear to be decoupled (Roberts et al., 2016). These contrasting results highlight the lack of constraints on the dynamical aspect of the water-masses mixing. In this paper, we combined grain-size distribution, clay mineralogy, and radiogenic isotope (Sr-Nd-Pb) analyses (on separated grain-size fractions) in order to investigate the evolution (horizontal and vertical extensions, pathways, speed) of deep-water-masses in the South Atlantic Ocean during the last termination.

2. General setting

2.1. Deep water-masses

Modern South Atlantic deep circulation is characterized by the incursion of the NADW into the Southern Ocean, where it mixes/interacts with both the AABW and the Circumpolar Deep Water (CDW; Fig. 1). The southward NADW mainly flows as Deep Western Boundary Current along the South American Margin before leaving the continental shelf and flowing eastward around 45°S (Reid, 1989; Larqué et al., 1997; Stramma and England, 1999). A branch of the NADW crosses the Atlantic Ocean at the equator before to flow southward along the African margin and to reach the Indian Ocean via the Good Hope Cape (Larqué et al., 1997). In the Southern Ocean, NADW flows between two parts of the CDW: the Upper Circumpolar Deep Water (UCDW) flows above, whereas the Lower Circumpolar Deep Water flows underneath. The northern extension of the UCDW is very asymmetric with larger extent in the eastern part of the South Atlantic (Larqué et al., 1997). On the west side of the Mid-Atlantic Ridge (MAR), the LCDW penetrates into the Argentine Basin via the Drake Passage and flows northward into the Brazil Basin (Speer and Zenk, 1993). On the east of the MAR, the LCDW is a major oceanic feature in the Cape Basin, where it becomes diluted in the Angola Basin (Larqué et al., 1997). The lower part of the LCDW is currently mixed with the upper part of the AABW (Orsi et al., 1999) that is produced heterogeneously along the Antarctic Shelf (Foster and Carmack, 1976; Orsi et al., 1999). Foster and Camarck (1976) demonstrated the formation of a very cold type of bottom water in the vicinity of the shelf break (the Polynyas mode) between 29 and 40°W and along the Antarctic Peninsula's tip, between 35 and 55°W and north of 65°S. Today this production occurs mainly in winter when seawater is close to freezing and becomes saltier due to sea ice formation (Foster and Camarck, 1976; Orsi et al., 1999), which increases its density and promotes convection. This mode is called the Polynyas mode. However, in the Weddell Sea, a second mode of bottom water formation occurs: the Ice Shelf Water mode, which corresponds to bottom water formation under the Antarctic ice shelves due to super-cooling (Krueger et al. and references therein, 2012). The AABW is very thick in the Weddell-Enderby Basin (more than 4000 m; Orsi et al., 1999) and is partially exported to the Argentine Basin via the eastern Scotia Sea (east and west of the South Sandwich Islands) toward the Brazil Basin via the Vema Channel, and to the Agulhas and Crozet basins (Stramma and England, 1999). The AABW is a dominant oceanic feature south of 50°S although its' northern influence extents to around 10°S (Reid, 1989).

The characteristics of deep water masses were not constant through time and the evolution of the AMOC is controversial (Weber and Drijfhout, 2007; Vázquez Riveiros et al., 2010; Waelbroeck et al., 2011; Howe et al., 2016). Some studies have suggested that during the Last Glacial Maximum (LGM) the NADW was as strong as today but shallower (Curry and Oppo, 2005; Gherardi et al., 2009). Other studies suggest that it was weaker and shallower (Menviel et al., 2012; Howe et al., 2016). The NADW southern extension seems limited during glacial times, whereas southern-born water-masses extended further north (Kuhn and Diekmann, 2002; Skinner et al., 2013). Similarly, modifications of the Antarctic Circumpolar Current (ACC, including the CDW) during the last climatic cycle are still debated. Some studies reported severe modifications of the ACC intensity in the Atlantic (Noble et al., 2012) and Indian (Dezileau et al., 2000; Mazaud et al., 2010) sectors of the Southern Ocean: the activity of the ACC increased during the LGM, probably linked to enhanced westerly winds (Dezileau et al., 2000; Walter et al., 2000; Mazaud et al., 2010). In contrast, other studies support insignificant modification of the ACC in the Atlantic sector of the Southern Ocean (Gersonde et al., 2003) and Drake Passage (McCave et al., 2014). Finally, the evolution of the AABW is also uncertain. Krueger et al. (2012) suggests that the production of AABW was similar during glacial and interglacial, but dropped during terminations (including the last deglaciation). In addition, Menviel et al. (2017) suggest that the "AABW" (corresponding to CDW and AABW in our study) was weaker during the LGM than today. In contrast, other studies suggest enhanced northward flow of AABW via deep western boundary currents in all three major ocean (Pacific: Hall et al., 2001; Govin et al., 2009; Indian: Govin et al., 2009; Atlantic: Govin et al., 2009; Spooner et al., 2018).

Any modifications of the AMOC have a potential effect on carbon storage/outgassing that is tightly controlled by ocean stratification/ventilation, itself resulting from contrasting physical and chemical

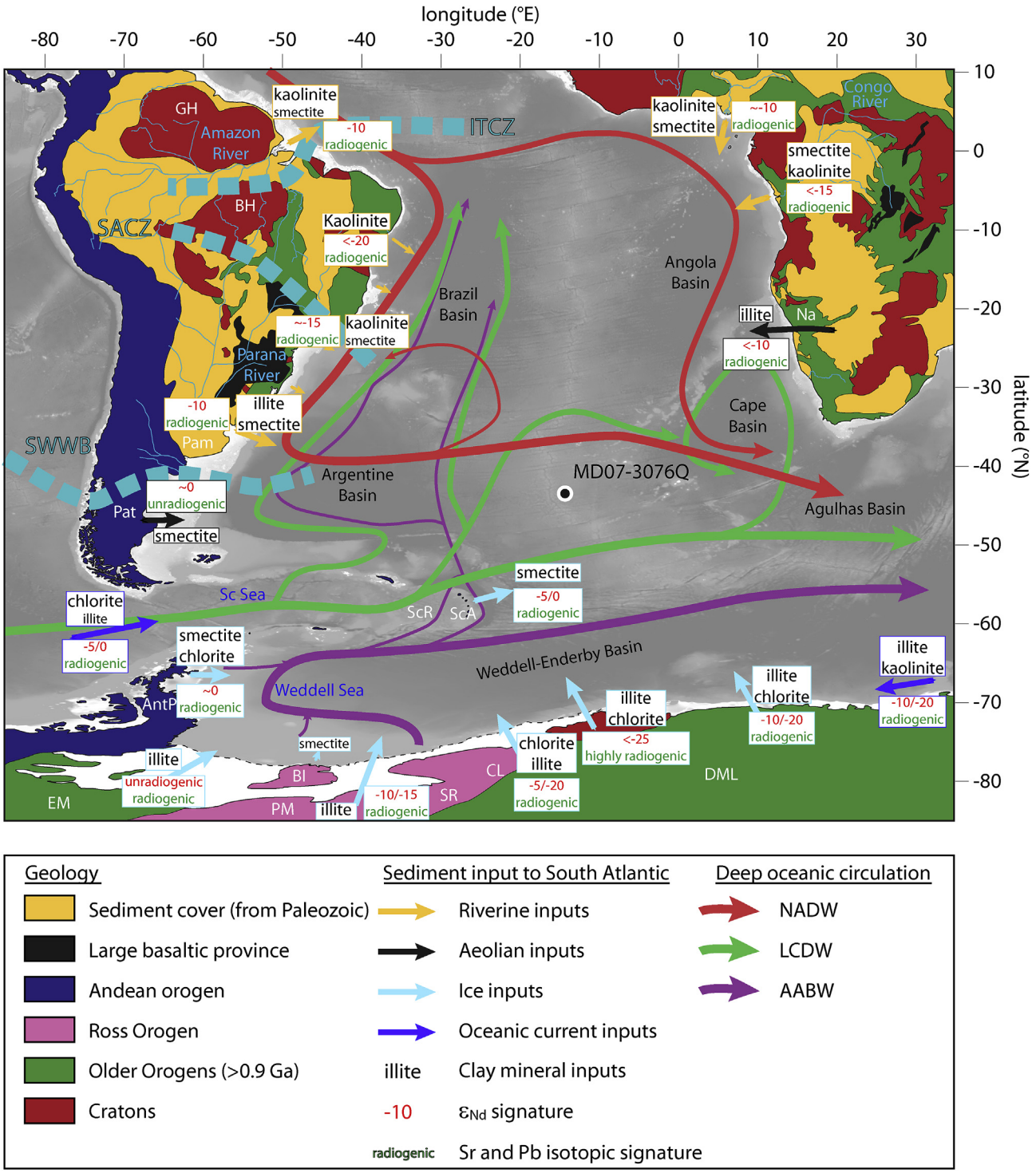

Fig. 1. Simplified geological map of the study area. Light blue text names riverine systems, dark blue text names seas, black text names oceanic basins, and white abbreviations names areas. In South America: Guyana Highlands -GH-, Brazilian Highlands -BH-, Argentinian Pampas -Pam-, Patagonia -Pat-; in Africa: Namibian deserts-Na-; in Antarctica: Ellsworth Mountains -EM-, Antarctic Peninsula -AntP-, Pensacola Mountains -PM-, Berkner Islands -BI-, Shackleton Range -SR-, Coats Land -CL-, Dronning Maud Land -DML-. Clay mineral inputs to the South Atlantic Ocean derived from the studies of Petschick et al. (1996); Diekmann et al. (2000); Walter et al. (2000); Guyot et al. (2007); Bayon et al. (2016); and Khondoker et al. (2018). (For interpretation of the references to colour in this figure legend, the reader is referred to the Web version of this article.)

properties of the water-masses. High ocean stratification – as during the last glacial – inhibits vertical mixing and isolates the deep ocean from the atmosphere. In contrast, ventilation events – breakdown of the stratification that occurred during the last deglaciation – allow CO_2 to upwell from the deep ocean and to be rapidly transferred to the atmosphere (Toggweiler et al., 2006; Barker et al., 2010; Skinner et al., 2010, 2013; 2014; Burke and Robinson, 2012).

2.2. Geological setting

The Atlantic sector of the Southern Ocean may receive

sediments from Antarctica, the Scotia Sea area (i.e., Scotia Arc, southern Patagonia, and northern Antarctic Peninsula) South America, and Africa. Here, we present the general geological structure of these areas, and their respective isotopic signatures (Fig. 1).

Antarctica corresponds to two distinct geological domains: East and West Antarctica. West Antarctica includes the Ellsworth Mountains (EM), the Antarctic Peninsula (Ant P), the Scotia Arc region (SCA). The geology of the Ellsworth Mountains (Fig. 1) is poorly known due to the lack of outcrop. These mountains are composed of Precambrian rocks, corresponding mainly to granodiorite orthogneiss intruded by granitic and pegmatitic sheets (Tingey et al., 1991). The isotopic composition of the area is not known, but the age of the rock suggests radiogenic Sr and Pb isotope ratios, and unradiogenic ε_{Nd} (Fig. 1). This area mostly delivers illite to the sea (Petschick et al., 1996, Fig. 1). The Antarctic Peninsula, composed of alkaline and calcalkaline magmatic rocks associated with deformed sediments of similar composition (Anderson, 1965; Tingey et al., 1991), is a potential source of terrigenous sediment for CDW and AABW. The Antarctic Peninsula is characterized by radiogenic ε_{Nd}, and low Sr and high Pb isotope ratios (Fig. 1). Clay minerals from this area mostly correspond to well-crystallized smectite (crystallinity around 1.5, Petschick et al., 1996, Fig. 1), and chlorite. The Scotia Arc islands rocks are similar to those of the Antarctic Peninsula but with slightly more radiogenic Nd, and slightly less radiogenic Sr and Pb (Fig. 1). This area exports exclusively well-crystallized smectite to the ocean (crystallinity lower than one; Petschick et al., 1996).

The East Antarctic domain is an old shield with rocks >0.9 Ga. Rocks from the Pensacola Mountains (PM) to the Shackleton Range (SR) represent the Ross Orogen (i.e., Transantarctic Mountains) and are mainly composed of varied metamorphic rocks aged from the Late Proterozoic to Late Paleozoic (Barrett, 1991; Laird, 1991; Tingey, 1991; Hauptvogel and Passchier and references therein, 2012). The isotopic composition of the area is characterized by unradiogenic Nd, with intermediate to high Sr isotope ratios (Fig. 1). The Pb isotope composition unknown, as is the case for most of East Antarctica rocks. The few studies reporting Pb isotope ratios have been carried out on feldspars only. The area releases mostly illite and chlorite (Petschick et al., 1996). Smectite is also exported from the Berkner Island, but is found only locally (Petschick et al., 1996). To the east, the Grenville Belts (920–1330 Ma) outcrop on the Coats Land (CL) and western Dronning Maud Land (WDML) with a wide range of gneissic and clastic sediments (Capurro, 1955; Anderson, 1965; Tingey et al., 1991) with unradiogenic Nd, and radiogenic Sr isotope ratios (Fig. 1). Clay minerals produced in this area are mainly chlorite and illite (Petschick et al., 1996). In the northernmost part of the Dronning Maud Land, the old Grunehogna Craton is composed mainly of Archean granitoids (Tingey et al., 1991; Mieth and Jokat, 2014; Pierce et al., 2014) with very unradiogenic Nd ($\varepsilon_{Nd} \ll -20$) and radiogenic Sr ratios (Fig. 1). The clay minerals generated in that area are mainly chlorite and illite (Petschick et al., 1996).

South America can be divided into two blocks: the recent Andean Orogen, and the old South American Shield. In the Atlantic Sector of the Southern Ocean, the Andean Orogen mostly corresponds to Patagonia (Pat). The geology and the isotopic composition of this region is similar with the Antarctic Peninsula: radiogenic Nd, unradiogenic Sr and Pb isotope ratios, but with higher $^{207}Pb/^{204}Pb$ than the Antarctic Peninsula (Fig. 1; Olivero and Martinioni, 2001; Sayago et al., 2001 and references therein; Smith et al., 2003; Khondoker et al., 2018). Even if the climate is slightly more humid than in the Antarctic Peninsula, Patagonia also produces mainly well-crystallized smectite (Petschick et al., 1996; Desiage et al., 2018; Khondoker et al., 2018).

The South American Shield is composed of several cratonic areas separated by vast ancient orogenic belts. (Cordani and Sato, 1999; Engler, 2009; Oyhantçabal et al., 2011; Siegesmund et al., 2011; de Alkmim, 2015). Cratonic areas are mainly composed of granitoids and a wide range of metamorphic rocks, while orogenic belts are composed of a large variety of metamorphic rocks with high original composition (from the granite to the ophiolite and the juvenile magmatic arc; Almeida et al., 1981; Barros et al., 1982; Moura and Gaudette, 1993; Neves, 2003; de Alkmim, 2015; Nogueira et al., 2007; Pimentel et al., 2011; Fuck et al., 2014; McGee et al., 2015; D'el-Rey Silva et al., 2016). The overall isotopic composition of the South American Shield is radiogenic Sr and Pb, and very unradiogenic Nd isotope ratios (Fig. 1). South of the South American Shield, a large tholeiitic-basaltic province is known as the Parana basalt (Waichel et al., 2012; Milani and Ramos, 2017). The composition of the Parana basalts differs from the South American Shield with radiogenic Nd, and very low $^{87}Sr/^{86}Sr$ ratio (<0.5; Tapani Rämö et al., 2016).

This South American Shield is drained by important riverine systems such as the Amazon and Parana rivers. The Amazon drains sediments from the Andes, as well as the South American Shield. The South American Shield is characterized by rocks with unradiogenic Nd and radiogenic Sr and Pb (Fig. 1). The clay mineral exported to the ocean is mainly kaolinite (Petschick et al., 1996; Guyot et al., 2007; Bayon et al., 2015). However, sediments are mainly exported northwards toward the Caribbean Sea. The Parana River drains the southern part of the South American Shield, the Parana basalts, and the north of Patagonia. Its isotopic composition has intermediate Nd, Sr, and Pb isotope ratios (Fig. 1). Clay minerals transported via this river are illite (~60%; Petschick et al., 1996; Campodonico et al., 2016), kaolinite, and smectite. Other smaller rivers drain the south of Brazil, and mainly deliver sediments characterized by unradiogenic Nd, and radiogenic Sr and Pb isotope ratios, containing mainly smectite derived from the Parana basalts and kaolinite (Fig. 1; Petschick et al., 1996). On the other hand, Patagonia and Pampas are dry and windy areas (Clapperton, 1993). Consequently, part of the detrital particles is exported to the ocean via aeolian processes as loess (Mathias et al., 2014). The overall isotopic composition of this smectite-rich loess is radiogenic Nd, unradiogenic Pb and Sr ratios. According to Mathias et al. (2014), the sediment delivery to the southwest Atlantic is currently dominated by loess, and by the Parana River sediments.

A large proportion of the African continent comprises Archean Cratons (western Africa, Congo), and rocks related to the Pan African Orogen. The cratons are composed of gneisses while the Pan African Orogen is mainly composed of flysch deposits associated with volcanic formations, and intruded by granitoids. The overall geochemical composition of Africa is intermediate to very unradiogenic Nd, and intermediate to very radiogenic Sr and Pb isotope ratios (Fig. 1). Clay minerals formed in the Congo depression are mainly poorly crystallized smectite and kaolinite, whereas the Namibian deserts release illite-rich loess (Bremner and Willis, 1993; Petschick et al., 1996; Bayon et al., 2015, Fig. 1).

3. Material and methods

3.1. Material

This study is based on sediment samples from core MD07-3076Q (44°9.2′S, 14°13.7′W) recovered by the French Vessel *Marion Dufresne* in 2007 on the eastern flank of the Mid-Atlantic Ridge at 3770 m depth (Fig. 1). The core chronology is based on planktonic foraminifer radiocarbon dates (30 measurements for the studied interval) and stratigraphic control points (Skinner et al., 2010, 2013; 2014; Gottschalk et al., 2015b). Today, the site is bathed in the

LCDW. From the seafloor to the surface, the water masses observed in the water column above the study site are the LCDW, NADW, UCDW, and intermediate and surface waters. In nearby deeper oceanic basins, the AABW is also found, and it is thought that particles transported by this bottom water can reach our site by advection and mixing with the LCDW.

3.2. Sample preparation and analytical procedure

All samples were first decarbonated using 0.1 N HCl and then deflocculated by repeated washing using pure water.

3.2.1. Grain-size distribution

Grain-size distribution was measured on carbonate-free sediment using a Malvern Mastersizer 2000 laser (0.02–2000 μm) following standard protocols (Montero-Serrano et al., 2009). The clay-size fraction corresponds to the proportion (in volume) of particles with a diameter smaller than 2 μm, the cohesive silts correspond to the 2–10 μm diameter particles, the sortable silts correspond to the 10–63 μm diameter particles, and the sand fraction to the particles coarser than 63 μm.

3.2.2. Clay mineralogy

The clay-size fraction (<2 μm) was isolated by differential settling according to Stoke's Law. This fraction was then concentrated by centrifugation (40 min, 3500 rotation per minute) and an aliquot was placed on glass slides. X-ray diagrams were obtained using a Bruker D4Endeavor (standard 30 kV and 30 mA). Each sample is run three times between 2.49 and 32.5°2θ: (1) dried sample, (2) glycolated sample (12 h in ethylene glycol), and (3) heated sample (490 °C for 2 h). The proportion of each clay mineral (smectite, chlorite, illite, and kaolinite) is determined using the main X-ray diffraction peaks (layer and interlayer) on X-ray spectra according to their crystallographic characteristics (Brown, 1980). Smectite is characterized by a main peak at 14–15 Å on the air-dried samples that expands at 17 Å after ethylene glycol saturation and collapses at 10 Å after heating. Illite is characterized by a main peak at 10 Å on the three runs. Kaolinite and chlorite are measured based on their main peak at 7–7.2 Å and further distinguished using pseudo-void deconvolution of the kaolinite/chlorite doublet at 3.54/3.58 Å. All measurements and semi-quantitative estimations are processed using the McDiff software (Petschick, 2000). The index of Esquevin (1969) corresponds to the ratio between the intensity of the peak of illite at 5 Å and at 10 Å (illite 5 Å/10 Å). In this study, the crystallinity of illite and smectite has been measured using the method of integral breath to enable comparison with the work of Petschick et al. (1996) in the South Atlantic. High crystallinity (high values of the index) corresponds to badly crystallized mineral.

3.2.3. Isotope analysis

The grain-size distribution recognized three distribution modes. These three grain-size fractions were then isolated in order to examine their provenance. The clay-size fraction (0–2 μm) was isolated by repeated extractions by settling. The coarse fraction (20–40 μm in the old section of the core before 11.5 ka cal BP, noted hereafter as ka, and 20–32 μm after 11.5 ka) was isolated by sieving the clay-free residue. The 2–20 μm grain-size fraction is thus the residue of clay separation and coarse fraction sieving. An aliquot of 10–150 mg (depending of the sediment quantities available) was then used for chemical procedures.

Chemical and isotopic measurements were performed at the Faculty of Science of the Vrije Universiteit, Amsterdam. Sediment was digested in closed Savillex™ Teflon beakers using a mixture of concentrated HF and HNO_3 (~2/3 and 1/3, respectively) for a few days at 120 °C. After digestion, samples were dried out and redissolved in ~6.5 N HCl to remove fluorides. Nd, Sr, and Pb were purified using conventional ion chromatography. Pb isotopes were processed first and purified using AG-X8 200–400 mesh resin. Light rare earth elements (LREE) were isolated using true-spec resin medium (Eichrom™, 100–150 μm mesh size) and Nd was eluted from the LREE fraction using LN-resin (Eichrom™, 50–100 μm mesh size). Sr was recovered using Sr resin column. Nd and Pb measurements were performed by bracketing using respectively CIGO and NBS981 standards on Thermo Scientific Neptune multi-collector inductive coupled plasma-mass spectrometer (MC-ICPMS), whereas Sr measurements were performed on a thermal ionization multi-collector-MS (TIMS). Due to relatively low content of Nd in some of the coarse grain-size fraction (20–32/40 μm), Nd measurements of these fractions were also performed by TIMS.

4. Results

4.1. Grain-size distribution

The grain-size distribution is bimodal throughout the core (Fig. 2) with a coarse mode ranging in the sortable silts fraction (from 23.6 to 36.2 μm, average: 30.4, standard deviation: 2.48; Table 1) and a fine mode ranging in the cohesive silts fraction (from 5.6 to 9.3 μm, average: 6.8, standard deviation: 0.8; Table 1). The sortable silt (10–63 μm) fraction is dominant (41–52% in volume of the total terrigenous fraction, average: 47%, standard deviation: 2.4; Table 1) and the cohesive silts (2–10 μm) represent 35–45% (average: 39%, standard deviation: 2.4; Table 1). The clay (<2 μm) and sand fractions (>63 μm) represent respectively 2–5% (average: 3.4%, standard deviation: 0.7; Tables 1) and 1 to 6% (average: 3.0, standard deviation: 1.0; Table 1) of the total terrigenous fraction (Table 1).

In details, the mean of the coarse mode (hereafter mentioned as the sortable silt mode) is slightly coarser during the LGM (Fig. 2a), and decreases during the deglaciation and reaches its minimum values after the Younger Dryas (YD). The average size of the fine mode (hereafter mentioned as the cohesive silt mode) is maximum at the end of the LGM and displays its lowest values during the deglaciation (Fig. 2b).

4.2. Clay mineralogy

The clay mineral assemblage is composed of smectite ((S) 18–59%; Fig. 3a), illite ((I) 21–40%; Fig. 3d), chlorite ((C) 12–33%; Fig. 3e), and kaolinite ((K) 5–14%; Fig. 3f) with higher smectite content at the end of the deglaciation, and higher illite, chlorite and kaolinite contents during the LGM. The smectite crystallinity ranges from 0.89 to 1.45 (Fig. 3b) and varies in phase with the smectite content with slightly higher variability between 25 and 30 ka. The illite crystallinity varies between 0.27 and 0.42 (Fig. 3c and 4) without major variation. Clay mineral proportions are relatively stable during the LGM but records a shift during the deglaciation with an increase of smectite compared to the other clay minerals. The smectite crystallinity varies simultaneously with smectite proportion changes. The K/C ratio is stable during the LGM, and increases during the deglaciation. The I/S ratio presents two maxima at the beginning of the record and at the end of the LGM, sharply decreases at the beginning of the HS 1, and steadily decreases during the deglaciation.

4.3. Radiogenic isotopes

Isotopic results are presented for the sortable silt mode fraction

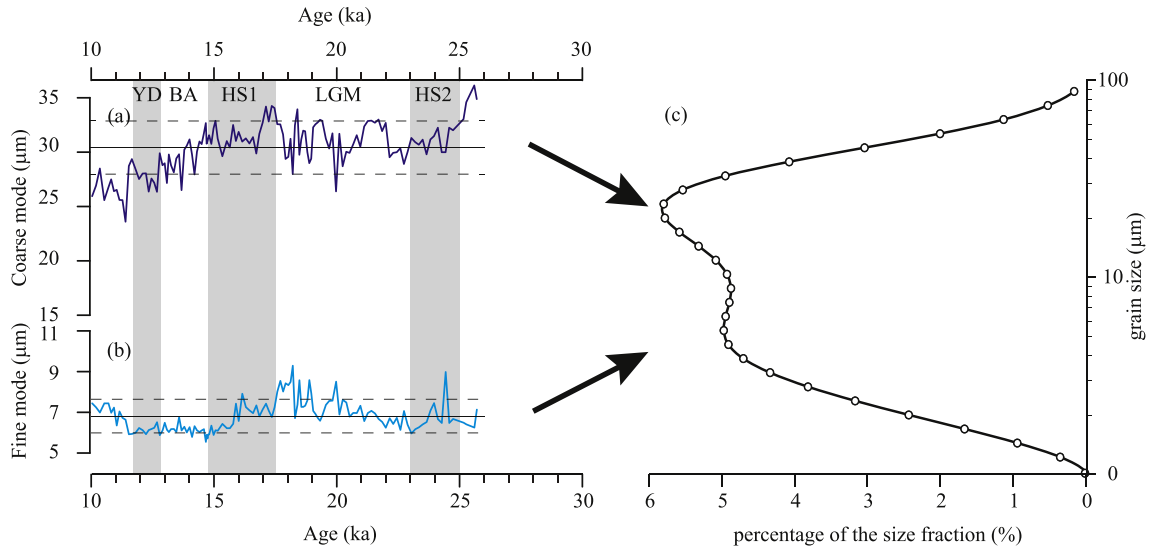

Fig. 2. Grain-size results from core MD07-3076Q. (a) and (b) Variation of the coarse and fine grain size mode values, respectively, through time. Black lines represent the average value for both grain-size modes while dashed lines represent their standard deviation; (b) typical grain-size distribution curve from the core MD07-3076Q. Two grain-size modes can be identified from the grain-size distribution curve. YD: Younger Dryas, BA: Bølling Allerød, HS: Heinrich Stadial; LGM: Last Glacial Maxima.

Table 1
Average values of the different proxies for the entire record, the LGM, and the deglaciation.

	average (10–30 ka)	LGM (25–17 ka)	Deglaciation (17–11.7 ka)	standard deviation (10–30 ka)
fine mode (μm)	6.8	7.2	6.3	0.8
coarse mode (μm)	30.4	31.3	30.4	2.5
clay fraction (%)	3.4	3.0	3.8	0.7
sortable silts (10–63 μm; %)	47.0	47.2	46.2	2.4
cohesive silts (2–10 μm; %)	39.4	38.8	40.2	2.4
sand (%)	3.0	3.5	2.6	1.0
smectite (%)	30.7	26.7	35.7	7.9
illite (%)	33.5	34.7	31.7	3.3
chlorite (%)	25.1	27.2	22.3	4.2
kaolinite (%)	10.6	11.4	10.3	1.3
I/S	1.2	1.3	0.9	0.3
K/C	0.4	0.4	0.5	0.1
ε_{Nd} (<2 μm)	−5.8	−5.0	−6.0	0.8
ε_{Nd} (fine mode)	−4.6	−4.6	−4.7	0.4
ε_{Nd} (coase mode)	−3.3	−1.8	−3.7	1.2
$^{87}Sr/^{86}Sr$ (<2 μm)	0.71130	0.71144	0.71136	0.00036
$^{87}Sr/^{86}Sr$ (fine mode)	0.70795	0.70800	0.70798	0.00019
$^{87}Sr/^{86}Sr$ (coase mode)	0.70889	0.70859	0.70926	0.00058
$^{208}Pb/^{204}Pb$ (<2 μm)	38.774	38.775	38.785	0.012
$^{207}Pb/^{204}Pb$ (<2 μm)	15.644	15.639	15.645	0.008
$^{206}Pb/^{204}Pb$ (<2 μm)	18.752	18.749	18.758	0.030

(20–32/40 μm) and the cohesive silt mode fraction (2–20 μm) and for the clay-size fraction (<2 μm) (Tables 2–4). Lead isotope ratios were only been measured on the clay-size fraction (Table 2).

4.3.1. Clay-size fraction (<2 μm)

The ε_{Nd} of the clay-size fraction ranges from −7.2 to −4.8. It is relatively stable during the last glacial (<± 0.5 ε_{Nd}), decreases by 2 ε units during the deglaciation and shows minimum values at the end of the deglaciation (Fig. 5c). The $^{87}Sr/^{86}Sr$ ratio ranges from 0.711 to 0.712: it is rather high and stable (<± 0.0003), during the last glaciation and displays a rapid decrease at ~15 ka. The ratio records a short rebound at 12.7 ka before reaching its minimum values at the end of the deglaciation (0.7107; Fig. 5d). The $^{87}Sr/^{86}Sr$ ratio and the ε_{Nd} show a similar temporal evolution (they both decrease during the deglaciation), which is surprising as in nature they usually record opposite relationship. The three Pb isotope ratios record their lowest values around 25 ka, and increase thereafter. This trend is more pronounced for the $^{207}Pb/^{204}Pb$ ratio during the deglaciation. Some fluctuations of the three ratios are observed during the deglaciation with higher ratios at climatic transitions (LGM/Heinrich Stadial 1 –HS1–, HS1/Bølling-Allerød – B-A –, B-A/Younger Dryas –YD–, Holocene onset), and low values during the middle of the HS1, the middle of the B-A, and the second half of the YD (except for the $^{206}Pb/^{204}Pb$). We note that the Sr isotope rebound observed at 12.7 ka is also associated with variations Pb isotope ratios.

4.3.2. Cohesive silt mode fraction (2–20 μm)

The ε_{Nd} of the 2–20 μm grain-size fraction (cohesive silt mode fraction) ranges from −5.5 to −3.9 with the lowest values at 13, 18, 23 and 29 ka (Fig. 5b). The $^{87}Sr/^{86}Sr$ ratios are generally constant with higher values around 13, 19, and 24 ka (Fig. 5f).

4.3.3. Sortable silt mode fraction: (20–32/40 μm)

The ε_{Nd} of the sortable silt mode fraction ranges from −4.9 to −1.4. Values are relatively unchanging during the last glacial period (−2 ± 0.5 ε_{Nd}) but decreases after 18 ka and reaches a minimum (−5) at the end of the deglaciation (Fig. 5a). The $^{87}Sr/^{86}Sr$

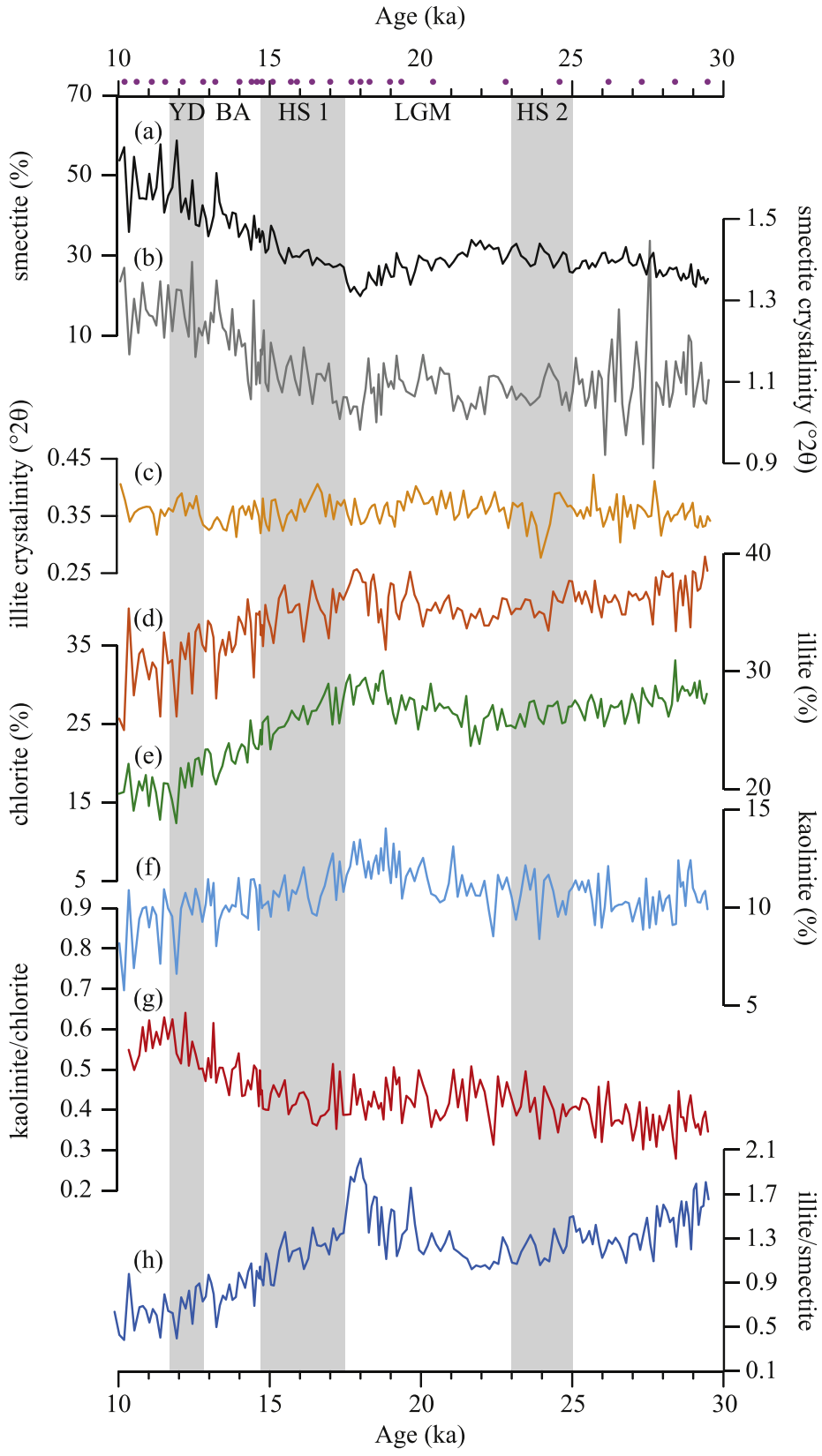

Fig. 3. Clay mineral data from core MD07-3076Q. Purple dots represent the radiocarbon dates used for the age model. (a) relative proportion of smectite (%); (b) smectite crystallinity (°2θ); (c) illite crystallinity (°2θ); (b) and (c) note that the lower is the crystallinity index, the better the mineral is crystallized; (d) relative proportion of illite (%); (e) relative proportion of chlorite (%); (f) relative proportion of kaolinite; (g) kaolinite/chlorite ratio (K/C); (h) illite/smectite ratio (I/S). (For interpretation of the references to colour in this figure legend, the reader is referred to the Web version of this article.)

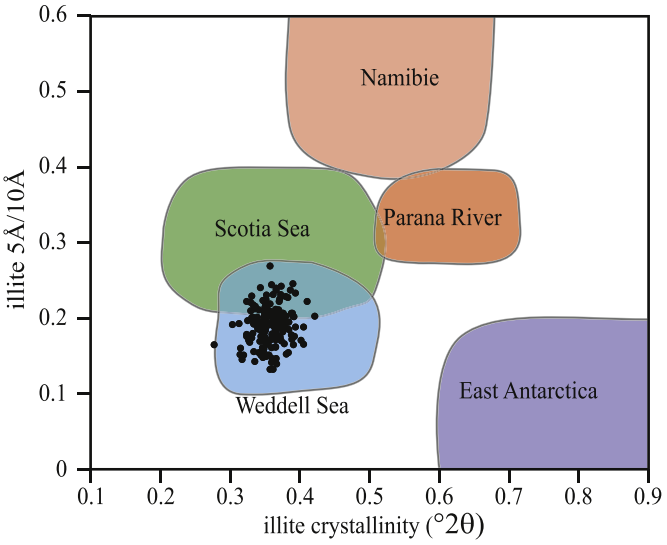

Fig. 4. Crystallographic properties of illite from site MD07-3076Q (black dots) and comparison with properties of illite from potential sources to the South Atlantic basin. The data used for comparison are from Petschick et al. (1996). Illite 5 Å/10 Å ratio gives information on the chemical properties of illite (Fe-Mg- vs Al-rich illite) while the crystallinity gives clues on the quality of the mineral crystal (high crystallinity: badly crystallized mineral).

ratio ranges from 0.708 to 0.710. $^{87}Sr/^{86}Sr$ values are lower during the HS 2, at the beginning of the HS 1, and at the beginning of the YD, while the highest value is recorded at the B-A offset (Fig. 5e).

5. Discussion

5.1. Sediment provenance

5.1.1. Clay size fraction: an overall provenance signal

To determine the provenance of this grain-size fraction, both clay mineral proportions and radiogenic isotopes have been used. Kaolinite and chlorite have distinct provenances: at present, kaolinite is mainly found at low latitudes where chemical weathering is strong. Brazilian rivers (Amazon and Parana), as well as equatorial and tropical African rivers are characterized by high contents of kaolinite (Fig. 1). Inherited kaolinite is also found in East Antarctica marine sediments (Fig. 1), but is transported by the westward Antarctic Coastal Current and remains trapped in the Weddell-Enderby Basin due to the Weddell Gyre circulation (Petschick et al., 1996) and this kaolinite is therefore unlikely to contribute to sedimentation at the studied site. Consequently, kaolinite can be used to trace the low latitude provenance. Conversely, presently, chlorite mainly characterizes high latitude regions, where weak chemical weathering allows its preservation. It is abundant in Antarctica and the Scotia Sea (Fig. 1). Consequently, chlorite can be considered a tracer of high latitude provenance. Thus, the kaolinite/chlorite ratio (K/C) discriminates southern-born versus northern-born material in the southern Atlantic (Petschick et al., 1996; Kuhn and Diekmann, 2002; Kruger et al., 2008).

Illite provenance is more complex. It is very abundant in the Weddell Sea, Namibian deserts, the Parana River (60% of the delivered sediment), and it is also present, although at lower concentrations (<30%), in the Scotia Sea (Fig. 1). To decipher the provenance of illite, we used the chemical (5/10 Å ratio, i.e., Fe-Mg vs. Al rich illite) and crystallographic properties (crystallinity) of this mineral. Data are compared with the 5/10 Å ratio and the crystallinity of illite of potential illite sources from the database of Petschick et al. (1996) (Fig. 4). This comparison demonstrates that the illite from core MD07-3076Q is similar to illite from the Weddell and Scotia seas while the chemical and crystallographic properties of the illite recovered at site MD07-3076Q is not compatible with a Namibian source. In the Scotia Sea, illite represents less than 30% of the total clay mineral fraction (from 10 to 30%; Petschick et al., 1996) and represents a mix of illite coming

Table 2
Isotopic composition from the clay size fraction (<2 μm) from sediment core MD07-3076Q. σ corresponds to the internal error.

Depth (cm)	Age (ka)	$^{143}Nd/^{144}Nd$	2σ	ε_{Nd}	$^{87}Sr/^{86}Sr$	2σ	$^{206}Pb/^{204}Pb$	2σ	$^{207}Pb/^{204}Pb$	2σ	$^{208}Pb/^{204}Pb$	2σ
51	10.03	0.512295	0.000006	−6.7	0.710814	0.000015	18.7555	0.0003	15.6553	0.0006	38.8083	0.0008
54	10.52	0.512286	0.000007	−6.9	0.710660	0.000010	18.7563	0.0003	15.6536	0.0006	38.7958	0.0008
57	10.91	0.512282	0.000005	−6.9			18.7438	0.0008	15.6562	0.0010	38.7993	0.0017
61	11.39	0.512282	0.000006	−6.9	0.710770	0.000011	18.7551	0.0003	15.6573	0.0006	38.8121	0.0007
62	11.52	0.512283	0.000005	−6.9	0.711048	0.000010	18.7685	0.0003	15.6482	0.0005	38.8027	0.0007
65	11.93	0.512293	0.000004	−6.7	0.710966	0.000007	18.7613	0.0003	15.6471	0.0005	38.7894	0.0006
68	12.33	0.512292	0.000006	−6.8	0.711240	0.000009	18.7640	0.0004	15.6490	0.0007	38.8070	0.0008
71	12.67	0.512302	0.000007	−6.5	0.711670	0.000012	18.7762	0.0003	15.6564	0.0006	38.8372	0.0008
74	12.98	0.512309	0.000005	−6.4			18.7648	0.0008	15.6530	0.0009	38.8073	0.0017
75	13.07	0.512340	0.000004	−5.8	0.711167	0.000011	18.7651	0.0003	15.6450	0.0005	38.7875	0.0008
80	13.56	0.512322	0.000004	−6.2	0.710987	0.000010	18.7374	0.0003	15.6419	0.0005	38.7535	0.0007
87	14.29	0.512325	0.000006	−6.1	0.710880	0.000010	18.7451	0.0005	15.6531	0.0007	38.7940	0.0013
92	14.69	0.512352	0.000006	−5.6	0.711540	0.000011	18.7593	0.0003	15.6414	0.0005	38.7803	0.0006
96	14.88	0.512352	0.000005	−5.6	0.711493	0.000010	18.7646	0.0003	15.6430	0.0005	38.7906	0.0007
101	15.51	0.512369	0.000006	−5.3	0.711706	0.000010	18.7565	0.0003	15.6363	0.0008	38.7654	0.0007
107	16.28	0.512375	0.000005	−5.1	0.711535	0.000009	18.7521	0.0003	15.6346	0.0007	38.7491	0.0007
112	16.97	0.512363	0.000005	−5.4	0.711769	0.000010	18.7548	0.0003	15.6410	0.0007	38.7640	0.0007
116	17.45						18.7601	0.0005	15.6471	0.0008	38.7896	0.0015
120	17.91						18.7530	0.0003	15.6461	0.0006	38.7800	0.0007
121	18.01	0.512381	0.000005	−5,0			18.7507	0.0003	15.6351	0.0007	38.7448	0.0006
130	18.79	0.512382	0.000005	−5,0			18.7428	0.0003	15.6406	0.0007	38.7479	0.0006
138	19.54	0.512373	0.000005	−5.2			18.7538	0.0003	15.6380	0.0007	38.7528	0.0007
149	21.10	0.512365	0.000004	−5.3	0.711683	0.000011	18.7444	0.0004	15.6378	0.0007	38.7508	0.0008
155	21.98	0.512362	0.000006	−5.4	0.711510	0.000010	18.7440	0.0006	15.6335	0.0010	38.7428	0.0021
160	22.72	0.512384	0.000005	−5,0	0.711400	0.000011	18.7397	0.0003	15.6349	0.0007	38.7399	0.0007
167	23.80	0.512394	0.000005	−4.8	0.711323	0.000012	18.7468	0.0004	15.6379	0.0008	38.7474	0.0007
173	24.72	0.512394	0.000004	−4.8	0.711286	0.000011	18.7424	0.0003	15.6355	0.0008	38.7328	0.0006
182	25.69	0.512394	0.000005	−4.8	0.711883	0.000010	18.7182	0.0003	15.6299	0.0007	38.6969	0.0006
196	27.27	0.512384	0.000004	−5,0			18.7321	0.0009	15.6445	0.0010	38.7522	0.0019
214	29.04	0.512360	0.000004	−5.4			18.7591	0.0009	15.6465	0.0011	38.7818	0.0019

Table 3
Isotopic composition from the sortable silt mode fraction (20–32/40 μm) from sediment core MD07-3076Q. σ corresponds to the internal standard error of the measurement.

Depth (cm)	Age (ka)	$^{143}Nd/^{144}Nd$	2σ	ε_{Nd}	$^{87}Sr/^{86}Sr$	2σ
51	10.03				0.708365	0.000009
55	10.69				0.708616	0.000008
57	10.91	0.512387	0.000006	−4.9	0.709192	0.000005
61	11.39	0.512403	0.000023	−4.6	0.708783	0.000013
63	11.64				0.709392	0.000005
65	11.93	0.512421	0.000006	−4.2	0.709592	0.000004
67	12.22	0.512416	0.000019	−4.3	0.708802	0.000010
71	12.67				0.707945	0.000005
73	12.89				0.709932	0.000006
75	13.07	0.512421	0.000007	−4.2	0.710185	0.000005
81	13.67	0.512425	0.000005	−4.1	0.709362	0.000005
87	14.29				0.709334	0.000009
91	14.65	0.512452	0.000005	−3.6	0.709046	0.000005
97	14.97				0.709254	0.000005
101	15.51	0.512491	0.000013	−2.9	0.708801	0.000007
107	16.28	0.512518	0.000005	−2.3	0.709632	0.000005
117	17.57				0.707884	0.000007
120	17.91				0.709324	0.000006
121	18.01	0.512567	0.000009	−1.4	0.708447	0.000005
122	18.10				0.708526	0.000006
131	18.87				0.708860	0.000008
137	19.40				0.708856	0.000009
144	20.37				0.709198	0.000006
145	20.51				0.708912	0.000009
149	21.10				0.709277	0.000007
153	21.69				0.708541	0.000008
155	21.98				0.708515	0.000010
160	22.72	0.512528	0.000005	−2.1	0.708235	0.000005
167	23.80				0.707873	0.000006
173	24.72				0.707796	0.000005
182	25.69	0.512533	0.000005	−2,0	0.708965	0.000005
196	27.27	0.512510	0.000008	−2.5	0.708907	0.000005
213	28.96				0.709026	0.000008

Table 4
Isotopic composition from the cohesive silt mode fraction (2–20 μm) from sediment core MD07-3076Q. σ corresponds to the internal standard error of the measurement.

Depth (cm)	Age (ka)	$^{143}Nd/^{144}Nd$	2σ	ε_{Nd}	$^{87}Sr/^{86}Sr$	2σ
51	10.03	0.512419	0.000006	−4.3	0.707880	0.000009
54	10.52	0.512395	0.000006	−4.7	0.707870	0.000012
57	10.91				0.707797	0.000005
61	11.39				0.708000	0.000009
65	11.93	0.512390	0.000007	−4.8	0.708190	0.000009
74	12.98	0.512370	0.000006	−5.2	0.708150	0.000009
74	12.98	0.512407	0.000008	−4.5	0.707662	0.000030
75	13.07	0.512393	0.000005	−4.8	0.708160	0.000009
80	13.56	0.512403	0.000006	−4.6	0.708010	0.000010
87	14.29	0.512417	0.000007	−4.3	0.707900	0.000010
96	14.88	0.512424	0.000007	−4.2	0.707730	0.000010
107	16.28	0.512396	0.000006	−4.7	0.708040	0.000009
112	16.97	0.512388	0.000006	−4.9	0.708000	0.000008
120	17.91	0.512379	0.000006	−5.1	0.707918	0.000008
121	18.01	0.512385	0.000005	−4.9	0.707975	0.000005
122	18.10	0.512355	0.000006	−5.5	0.708052	0.000011
130	18.79	0.512413	0.000006	−4.4	0.708370	0.000010
138	19.54	0.512420	0.000005	−4.2	0.707710	0.000010
149	21.1	0.512437	0.000005	−3.9	0.707890	0.000008
155	21.98	0.512409	0.000006	−4.5	0.707850	0.000009
160	22.72	0.512377	0.000006	−5.1	0.707930	0.000011
167	23.80	0.512435	0.000005	−4,0	0.708240	0.000013
173	24.72	0.512430	0.000006	−4.1	0.708110	0.000009
182	25.69				0.707816	0.000005
196	27.27	0.512401	0.000006	−4.6	0.707607	0.000008
214	29.04	0.512371	0.000005	−5.2		

from the Weddell Sea embayment via the AABW, and illite from the Pacific sector of Antarctica delivered by the CDW (Diekmann et al., 2000; Walter et al., 2000; Petschick et al., 1996). Importantly, in the Weddell Sea, illite represents at least 50% of the total clay mineral fraction (more than 80% in some areas; Petschick et al., 1996). Consequently, the Weddell Sea embayment is considered as the major, source of illite for our studied site.

Smectite has several potential provenances: the Angola Basin, southern South America, Scotia Sea Islands, and Antarctic Peninsula. The crystallinity of this mineral was measured in order to decipher its provenance. The well-crystallized smectite (low crystallinity; Fig. 3) is compatible with a provenance from southern South America (Pampas and Patagonia), Scotia Arc, or Antarctic Peninsula, which are all characterized by crystallinity lower than 1.5 (Petschick et al., 1996, Fig. 3). It rules out a contribution of poorly crystallized smectite (crystallinity > 2; Petschick et al., 1996) from Angola. In detail, the crystallinity of the smectite from our studied site likely corresponds to a mix between two types of sources: (1) Patagonia and Antarctic Peninsula with a crystallinity of 1.5; and (2) Scotia Arc with a crystallinity lower than 1.0. Interestingly, the proportion and crystallinity of smectite record very similar variations that suggest a dominant and rather continuous flux of smectite from the Scotia Arc (low crystallinity - ~1.1) during the last glacial period, with a supplementary supply of less well crystallized smectite (slightly higher crystallinity – 1.5; ~20%) from Patagonia or Antarctic Peninsula during the deglaciation (Supplementary Figs. S1 and S2).

In summary, both the proportions of the clay minerals and their crystallographic properties suggest that kaolinite mainly derives from low latitude areas, chlorite originates from Antarctica and the Scotia Sea, while illite mainly derives from the Weddell Sea embayment and smectite is derived from several sources (Scotia Arc, Patagonia, and Antarctic Peninsula). Moreover, mineralogical and crystallographic properties exclude Africa as a source of clay minerals consistent with the dominant westward oceanic circulation in the ACC (Fig. 1).

The coupled ε_{Nd} - $^{87}Sr/^{86}Sr$ isotope variation of the clay-size fraction (Fig. 6) reveal a mixed provenance between young sources around the Scotia Sea (Scotia Arc, Antarctic Peninsula, Patagonia) and southern South America (Patagonia and Pampas), and an old source from East Antarctica or the South American Shield (i.e., Brazil and Parana River).

The coherent Pb isotope variations in Fig. 7 support this interpretation recording a mix between the Antarctic Peninsula, Scotia Arc, and South American Shield. However, since very few data are available for the Pb isotope compositions of East Antarctica, a contribution from this area cannot be excluded. The three isotopic systems suggest an increased contribution of older material during the deglaciation compared with the LGM. Based solely on Nd and Pb isotope data, it is rather difficult to distinguish South America and East Antarctica as the old end-members during the deglaciation. However, the increase of the K/C ratio during the deglaciation supports the hypothesis of enhanced relative contribution from the South American Shield.

5.1.2. Cohesive silt mode fraction (2–20 μm)

Both $^{87}Sr/^{86}Sr$ and ε_{Nd} of the cohesive silt mode fraction record limited variation throughout the deglaciation (Fig. 5). The isotopic results indicate that the provenance is located in Patagonia and in the Antarctic Peninsula, with an additional contribution of old source (South American Shield and/or East Antarctica). These results suggest that no major modification of provenance occurred during the deglaciation. Strontium and Nd isotope ratios do not allow discrimination of the source of old material for the cohesive silt mode fraction. The Nd isotope ratios suggest on average a

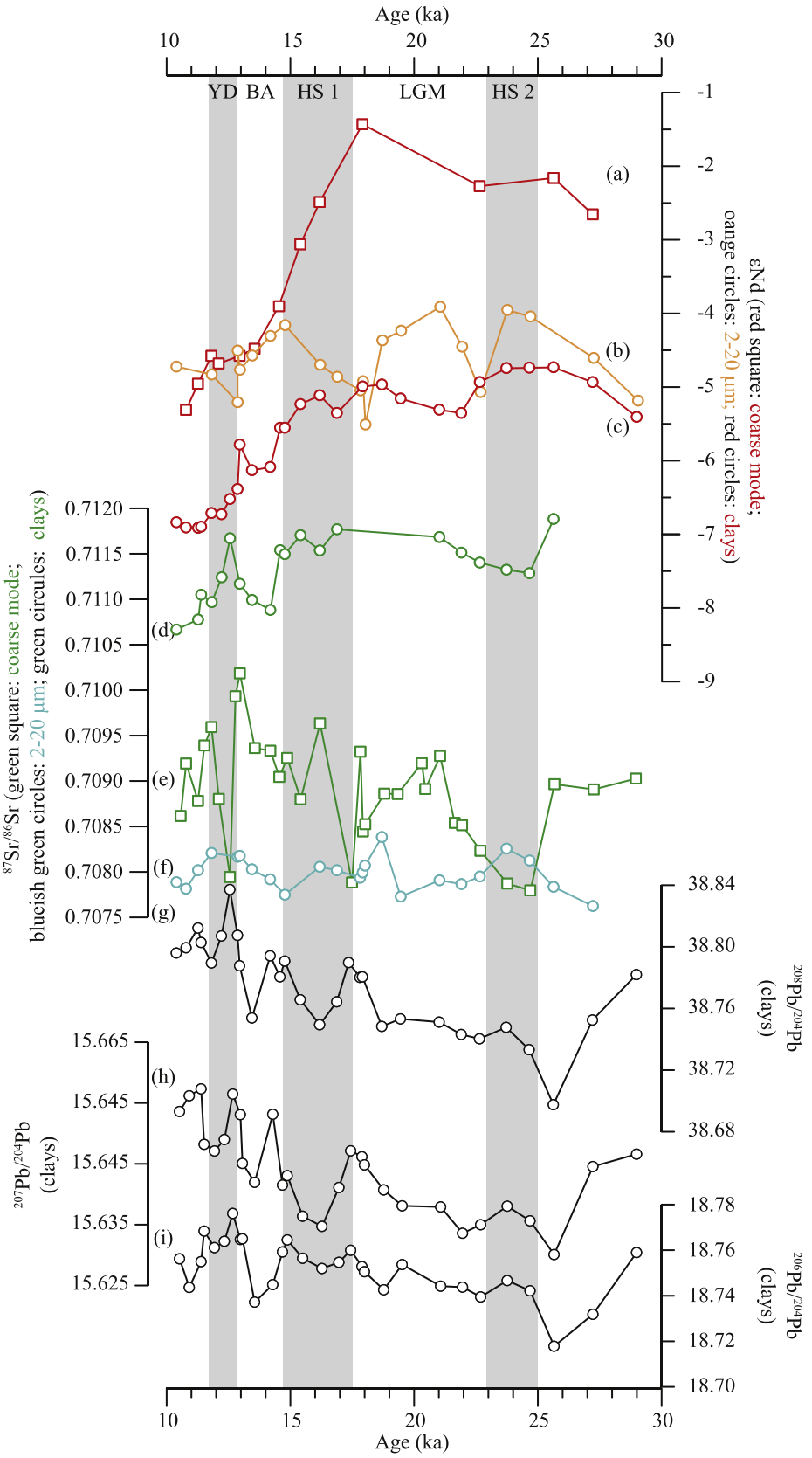

Fig. 5. Isotopic results from core MD07-3076Q. (a) ε_{Nd} from the sortable silt mode fraction (20–32/40 μm); (b) ε_{Nd} from the cohesive silt mode fraction (2–20 μm); (c) ε_{Nd} from the clay-size fraction (<2 μm); (d) $^{87}Sr/^{86}Sr$ from the clay-size fraction (<2 μm); (f) $^{87}Sr/^{86}Sr$ from the sortable silt mode fraction (20–32/40 μm); (g) $^{87}Sr/^{86}Sr$ from the cohesive silt mode fraction (2–20 μm); (h) $^{208}Pb/^{204}Pb$, (i) $^{207}Pb/^{204}Pb$, and (j) $^{206}Pb/^{204}Pb$ from the clay-size fraction (<2 μm).

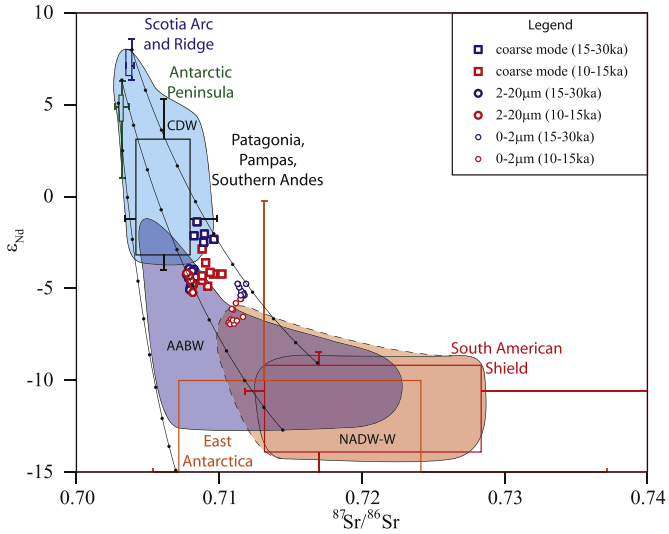

Fig. 6. $^{87}Sr/^{86}Sr$-ε_{Nd} diagram of MD07-3076Q sediments and of potential sources of sediments for the South Atlantic Basin. Boxes representing the reference data delimit the first and the third quartile. The median values are represented by horizontal and vertical lines attached to the boxes for the ε_{Nd} and the $^{87}Sr/^{86}Sr$ ratios, respectively. The short strokes at the end of these lines represent the 10th and 90th percentile values. Accordingly, the box represent 50% of values found for each potential provenance, and 80% is represented with the lines. Data sources: South American Shield- Allègre et al. (1996); Basile et al. (1997); Walter et al. (2000); de Mahiques et al. (2008); Jeandel et al. (2007), and references therein; Mallmann et al. (2007); Ganade de Araujo et al. (2014); Fuck et al. (2014); -Patagonia, Pampas, Southern Andes- Stern et al. (1990); Grousset et al. (1992); Basile et al. (1997); Walter et al. (2000); Smith et al. (2003); Jeandel et al. (2007), and references therein; Khondoker et al. (2018); -Scotia Arc and Ridge- Jeandel et al. (2007); Harrison et al. (2003); -Antarctic Peninsula- Hole et al. (1993); Kosler et al. (2009); Roy et al. (2007); Lee et al. (2005); -East Antarctica- DePaolo et al. (1982); Luttinen et al. (1998, 2010); Roy et al. (2007); Will et al. (2010).

higher radiogenic contribution for cohesive silts compared with the clay-size fraction (Fig. 6).

5.1.3. Sortable silt mode fraction (20–32/40 μm)

Both Sr and Nd isotope ratios of the sortable silt during the LGM record one dominant provenance: the Scotia Sea area (Patagonia, Scotia Arc, Antarctic Peninsula; Fig. 5). During the deglaciation, an important shift to less radiogenic ε_{Nd} values (4 units) is observed implying an increased contribution of an older end-member such as East Antarctica and/or the South American Shield. However, because East Antarctica and the South American shield have similar Sr and Nd isotope composition, it is not possible to distinguish them with these isotopes (Fig. 6). Consequently, investigating the main transportation patterns is necessary to identify the source of old material for both the cohesive (2–20 μm) and the sortable silt mode fractions (20–32/40 μm).

In summary (Fig. 6), all three grain-size fractions compositions are located between two end-members: the Scotia Sea-southern South America area (Antarctic Peninsula, Scotia Arc and Ridge, Patagonia, Pampas, Southern Andes), and crustal shields (East Antarctica, South American Shield). The clay-size fraction appears the most crustal-like, whereas the sortable silt mode presents the most mantle-like composition. The 2–20 μm grain-size fraction presents the lowest $^{87}Sr/^{86}Sr$, meaning that the difference with the other grain size fraction is related to distinct provenances rather than grain size effect. Both the clay size and the sortable silt mode fractions display an increase of the crustal end-member. In the clay size fraction, clay mineralogy enabled the identification of this old crustal source (i.e., the South American Shield).

5.2. Transportation pattern and palaeoclimatic implications

The provenances of the sediments for the three distinct grain-size fractions have been identified (or partially identified) in the previous section using their mineralogical and geochemical characteristics. Now, we will focus on identifying their transportation patterns and vectors from the source to the sedimentation site.

Several studies propose that aeolian processes may lead to significant particle transfers from Patagonia into the central Atlantic sector of the Southern Ocean (Hegner et al., 2007; Desiage et al., 2018). The aeolian contribution of loess from Patagonia was enhanced during the LGM as far as Antarctica (Petit et al., 1990; Grousset et al., 1992; Diekmann, 2007; Lambert et al., 2008).

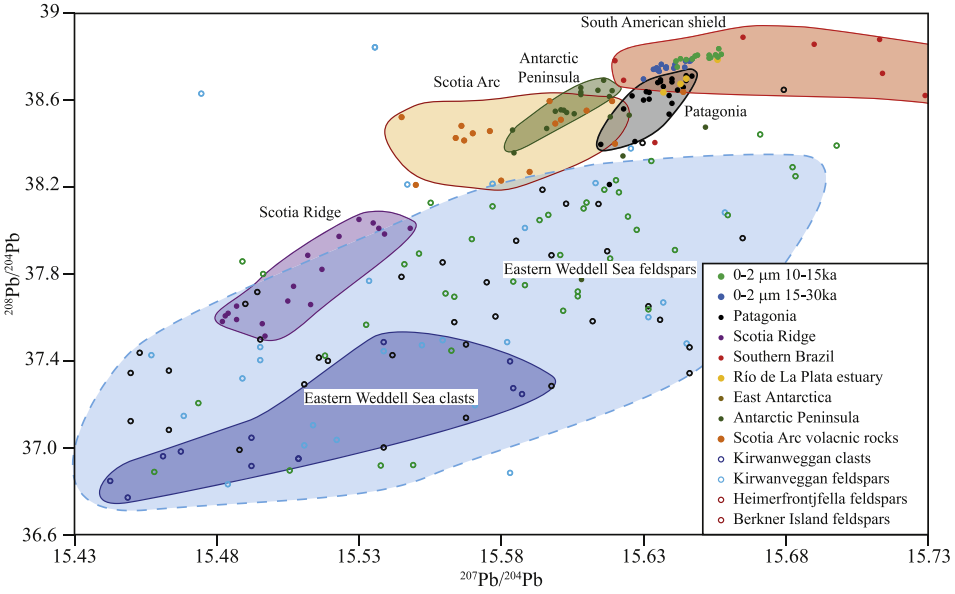

Fig. 7. Pb isotope composition of core MD07-3076Q and of potential sources of sediments. The reference data used for comparison are from Fretzdorff et al. (2002), -Scotia Ridge-; Khondoker et al. (2018), -Patagonia-; Cohen and O'Nions (1982); Barreiro (1983), -Scotia Arc-; Lee et al. (2005), Košler et al. (2009), Flowerdew et al. (2012) -Antarctic Peninsula-, de Mahiques et al. (2008), -South American Shield-; Flowerdew et al. (2012), -Eastern Weddell Sea-.

Although this hypothesis could be supported by the radiogenic Nd signal observed in both the clay-size and the sortable silt mode fraction during the LGM, the mineralogical of MD07-3076Q sediments is not in agreement with an enhanced contribution from Patagonia. The dominant clay mineral in Patagonia is smectite (up to 95%), and the contribution of Patagonian smectite in our clay-size fraction is lowest during the LGM (Fig. 3). Consequently, direct aeolian inputs cannot be significant at our site, and oceanic currents appear to be the main contributors to sedimentation (Moriarty, 1977; Petschick et al., 1996; Kuhn and Diekmann, 2002). This means that any aeolian particles from Patagonia delivered to the southwest Atlantic (Mathias et al., 2014) likely reach our site via oceanic transport processes.

The size of particles transported by water flow is directly related to the flow energy, with size increasing with the flow speed. This property was used in previous studies to track the temporal evolution of paleo-current flow (e.g. McCave and Hall, 2006; McCave and Andrews, 2019). Below we show that the different grain-size modes not only correspond to distinct flow speeds, but specific water mass at site MD07-3076Q. Consequently, grain-size modes (2–20 μm and 20–32/40 μm) can be associated to specific deep-water-masses.

The clay-size fraction (i.e., the <2 μm particles) with very high specific surface readily floats and hence can undergo long-range transportation (>500 km). Consequently, particles within this grain-size fraction can be used to record the relative contribution of the main deep-water masses.

5.2.1. Clay-size fraction: the distant terrigenous signal

The NADW carries fine suspended particles from as far as the Labrador Sea. However, this signal is probably overprinted by the supply of sediments from more proximal sources such as Africa or South America. The western branch of the NADW (NADW-W; i.e., Deep Western Boundary Current) can transport sediments from Brazil, Parana River, Pampas, and Patagonia (Fig. 1). Both mineralogical and geochemical compositions of the particles transported by the western branch of the NADW are likely controlled by the southern extension of the water-mass. Currently the western branch drifts away from the South American coast around 45°S. This southern extension likely changed during the last glacial period and deglaciation (Skinner et al., 2010, 2014; Vásquez-Riveiros et al., 2010; Waelbroeck et al., 2011; Gottschalk et al., 2015a,b; Howe et al., 2016). Depending on its southern extent, the NADW is thus able to carry either mostly kaolinite (equatorial Brazil), or kaolinite and smectite (southern Brazil), or illite (Parana River basin), or well-crystallized smectite (crystallinity ~1.5; Patagonia). As shown above, the ε_{Nd} signature of these sediments is more radiogenic when the NADW extends further south (−20 in equatorial Brazil, to ~0 in Patagonia) while the Pb and Sr yield a slightly less radiogenic signature (Figs. 6 and 7).

The CDW transports sediments from the Scotia Sea area, including Scotia Arc, Patagonia, and the Antarctic Peninsula, as well as from the Weddell Sea when mixing occurs between the lower part of the LCDW and AABW. Then particles transported by the CDW likely record a younger isotopic signature (i.e., more radiogenic ε_{Nd} and unradiogenic Sr and Pb isotopes), and a mineralogical composition dominated by smectite and chlorite, while additional contribution of old material (unradiogenic ε_{Nd} and radiogenic Sr and Pb isotopes) and illite is possible when the LCDW and AABW mix together. In summary, illite is considered as injected into the sedimentary system via the AABW through mixing processes between LCDW and AABW while smectite and chlorite are likely transported by the CDW.

The AABW in the Atlantic sector mainly forms in the Weddell Sea embayment (Orsi et al., 1999), and thus, must carries sediments from its drainage basin (East Antarctica, Antarctic Peninsula), but may also transport sediment winnowed on its pathway such as the Scotia Arc or southern Patagonia in the Argentine Basin. The main clay minerals in the Weddell Sea embayment are illite associated with chlorite. Smectite may be injected in the AABW at the vicinity of the Scotia Arc. Kaolinite is almost absent in both the Weddell Sea embayment and the Scotia Sea area (Patagonia, Antarctic Peninsula and Scotia Arc) and is unlikely to be transported by the AABW. The isotopic composition of fine particles transported by the AABW ranges between two end-members: the very old sediments from East Antarctica ($^{87}Sr/^{86}Sr > 0.72$; $\varepsilon_{Nd} < -20$), and younger material from the Antarctic Peninsula and the Scotia Arc ($^{87}Sr/^{86}Sr \sim 0.70$; $\varepsilon_{Nd} > -5$; intermediate Pb isotope ratios). Consequently, the composition of particles transported by the AABW flowing out of the Weddell Sea is intermediate, with ε_{Nd} around −9 (Walter et al., 2000), and is potentially enriched in young material when entering the Scotia Sea.

The above observations are summarized in Table 5, in which specific isotopic and mineralogical signatures are associated to each deep water mass. It is clear that the K/C ratio as well as the ε_{Nd} composition reflect northern-versus southern-born water mass contributions (i.e., NADW versus CDW and AABW). Similarly, smectite and illite are transported by distinct water-masses and the illite/smectite ratio (I/S) can efficiently distinguish the AABW from the other water-masses. Thus, this ratio will further be used as a tool for estimating the AABW contribution through time.

The illite/smectite and kaolinite/smectite ratios have been plotted in Fig. 8. The three end-members for AABW, CDW and NADW are plotted according to the clay composition of their suspended loads. Fig. 8 highlights how the relative contribution of the three water masses (i.e., AABW, CDW, and NADW) to clay deposition has changed with time since the LGM. To interpret this figure it is important to keep in mind that changes observed in the contribution one deep water mass are relative compared to the other water masses. To construct Fig. 8 b, the proportion of clay particles deposited by each deep water mass was calculated as described below.

End-member deep water mass compositions were calculated from the average composition of deep water-masses shown in Fig. 8 a. Weights are computed as the inverse of the distance between the position of water-mass end-member (x_w;y_w) with $x_w = K/C_w$ and $y_w = I/S_w$ and the position of the data point (x_d;y_d), with $x_d = K/C_d$ and $y_d = I/S_d$ taken from the graph (Fig. 8a) for each water-mass: $W_w = 1/[\ (x_d\text{-}xw)^2+(y_d\text{-}y_w)^2]^{1/2}$. The position used for the deep water masses are: $xA_{ABW} = K/C_{AABW} = 0.3$; $y_{AABW} = I/S_{AABW} = 2.5$; $x_{CDW} = K/C_{CDW} = 0.1$; $y_{CDW} = I/S_{CDW} = 1$; $x_{NADW} = K/C_{NADW} = 0.9$; $y_{NADW} = I/S_{NADW} = 1$. The values used for the NADW correspond to the mineralogical composition of the NADW during the LGM. As a result, the contribution of NADW to the deposition of clay particles is underestimated (~10%) at the end of the deglaciation while the contribution of the CDW is overestimated (~10%). This choice does not have a strong impact on the contribution of the AABW (less than 4.5%). Second, the percentage of the contribution of each

Table 5
Synthesis of the mineralogical signature of the sediment transported by the three main deep water-masses. Crosses are given when increased delivery from a specific deep water mass increase the relative proportion of the clay mineral. As an example, it can be read as followed: "an enhanced delivery of terrigenous sediment from CDW increases the proportion of smectite and chlorite at site MD07-3076Q".

	smectite	illite	kaolinite	chlorite
NADW-W	X		X	
CDW	X			X
AABW		X		X

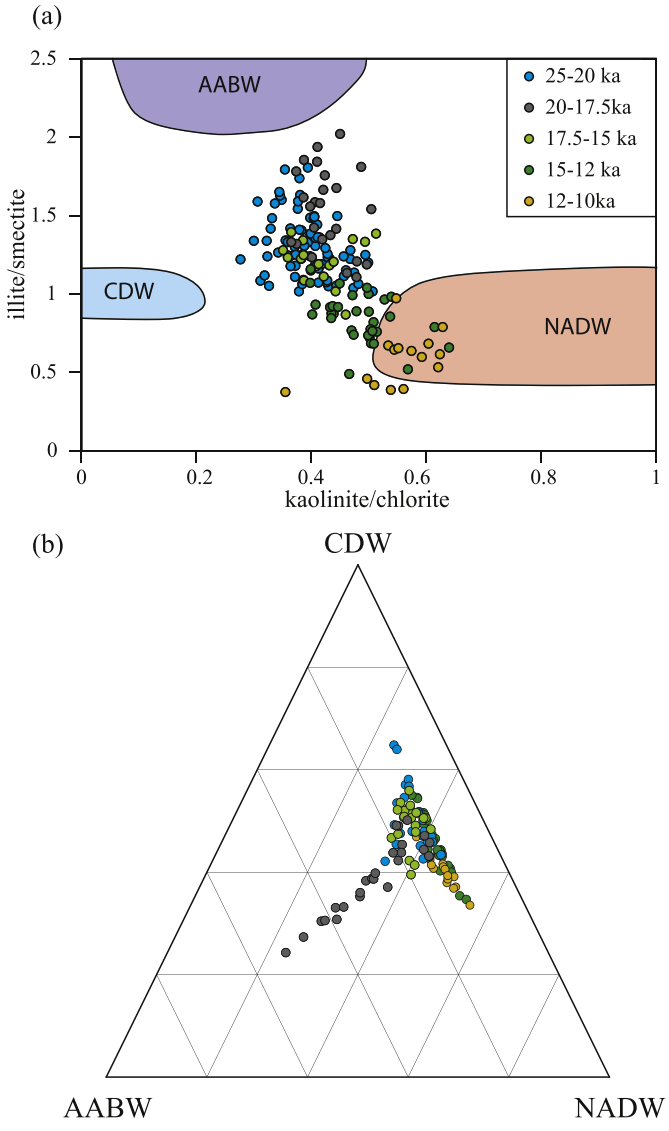

Fig. 8. (a) Plot of kaolinite/chlorite vs illite/smectite ratios from core MD07-3076Q from 25 to 10 ka. The composition of deep-water masses has been determined using the data from Petschick et al. (1996). (b) Ternary diagram comparing the contribution of the three deep water masses to the clay deposition at site MD07-3076Q.

water mass is calculated by bringing the sum of the weights computed to 100: [NADW's contribution] = W_{NADW}/(W_{NADW} + W_{CDW} + W_{AABW}) x 100.

To test the validity of this method to reconstruct the evolution of the past deep circulation, we compared our results with those of other water-masses proxies (e.g. seawater ε_{Nd} and $\delta^{13}C$). However, these latter methods proved incapable of distinguishing AABW from CDW. Consequently, we based the comparison on the proportion of the NADW compared to the southern sourced deep waters. Based on data from the same core, our estimates give comparable results to these two proxies (see Table 6). This suggests that our approach successfully reconstructs the evolution of these three deep water masses. However, our estimate of the proportion of the NADW is higher than the estimate of Howe et al. (2016) based on ε_{Nd}. This discrepancy can be explained by two factors. First, we were unable to make corrections for concentration differences of particles in the three deep water masses (i.e., quantity of clay particles per volume of water) due to the large uncertainties involved. In addition, it is very likely that the NADW is more concentrated in clay particles than the AABW and CDW due to sediment source effect (e.g., dry East Antarctica below thick ice sheets vs. humid South America highly drained by equatorial rivers). Consequently, even though our tool successfully reconstruct the variations of the NADW, the contribution of NADW is probably overestimated. In other words, our estimate of NADW contribution to the clay deposition is likely higher than the proportion of NADW (in volume of water). Second, the choice of the end member for the seawater ε_{Nd} of AABW + CDW made by Howe et al. (2016) is debatable (−5.5 during the LGM, −8.5 during the Holocene). Skinner et al. (2013) used a compositional end-member between −5 and −2, which yields a better match with the isotopic composition of seawater Nd at our site (−5.5, Skinner et al., 2013). Therefore, the estimate of Howe et al. (2016) appears to underestimate the contribution of NADW at our site.

From 25 to 20 ka, the CDW is clearly dominant, with a contribution of 50% on average, while the NADW and AABW deliver 35% and 15% of the clay fraction, respectively. The highest contribution of the AABW is observed at the end of the LGM between 20 and 17.5 ka (27% in average, but up to 52% at 18 ka). During this interval, the NADW and CDW deliver respectively 34% and 39% on average. At the end of this period, the mineralogical composition of the fine sediments deposited at site MD07-3076Q suggests that the AABW was dominant. At the beginning of the deglaciation, between 17.5 and 15 ka (i.e., during HS 1), the clay mineral composition of core MD07-3076Q indicates a decreased relative contribution of the AABW end-member (15% on average) associated to an increase of the relative contribution of the CDW (49%) end-member. This observation of an increase of the CDW contribution is supported by the radiogenic ε_{Nd} of the clay-size fraction and a $^{87}Sr/^{86}Sr$ close to the Scotia Arc composition (Figs. 5 and 6).

From 15 ka on, the clay mineral composition at the study site records an increasing contribution of the NADW until the end of the deglaciation (at least 47% for the interval 10–12 ka, Fig. 8). Compared with the LGM this suggests enhanced contribution of the NADW with reduced contributions from the CDW (40% for the interval 10–12 ka) and AABW (13% for the interval 10–12 ka). These results are strongly supported by the sharp decrease in ε_{Nd} and by the concomitant increase of $^{208}Pb/^{204}Pb$ and $^{207}Pb/^{204}Pb$ ratios from the clay size fraction (Figs. 5 and 7). This corroborates the conclusions based on the *cibicides* $\delta^{13}C$ measured in the same core (Fig. 9 e, Waelbroeck et al., 2011). In addition, increasing inputs of less crystallized smectite (slightly higher crystallinity: ~1.5, Supplementary Fig. S1) from Patagonia support the southward penetration of the NADW in the southern Atlantic Ocean, consistent with an increasing contribution of the NADW-W to sedimentation at site MD07-3076Q. Interestingly, the transition between B/A (that starts simultaneously with the southern Hemisphere cooling, the Antarctic Cold Reversal) and the YD appears to have no effect on the relative contribution of deep water masses and shows a continuous increase of the relative contribution of the NADW during these two periods.

Overall, the clay size fraction demonstrates that the contribution of the three deep water-masses changed through time. An increase of contribution of the AABW is recorded at the end of the LGM and is followed by a two-step deglaciation. First, an important reduction of the AABW is observed at the HS 1 onset. Second, an increase in the NADW contribution compared to the CDW is observed during the B/A and YD.

5.2.2. Cohesive silt mode fraction (2–20 μm): an AABW signal

According to our geochemical data, the provenance of the cohesive silt fraction is dominated by sources from the Scotia Sea area, especially Patagonia and Antarctic Peninsula, and by an old, unidentified, crustal source. According to the modern deep oceanic

Table 6
Correlation factors (R^2) between deep water mass proxies and the contribution of NADW to clay mineral deposition. All the data comes from the same sediment core (MD07-3076Q) and only samples from the same intervals (i.e. same depth) have been used to calculate the correlation factors. The correlation factor between the ε_{Nd} from clay particles and the ε_{Nd} from sea water is also high (higher than 0.8), but we chose not to report it in the table because of the low number of samples measured on the same interval (n = 6 instead of at least 14).

	NADW contribution to clay deposition (calculated using Holocene end member)	NADW contribution to clay deposition (calculated using LGM end member)	ε_{Nd} (clay)
cibicides $\delta^{13}C$	0.74	0.64	0.84
ε_{Nd} (seawater)	0.81	0.64	–

circulation, only the CDW and AABW are able to transport sediment from the Scotia Sea to the studied site (Fig. 1). It was also likely the case during the LGM and deglaciation. The AABW and CDW were likely spreading further north while the NADW was likely shallower, and retreated to the north (Kuhn and Diekmann, 2002; Barker et al., 2010; Waelbroeck et al., 2011). These modifications do not affect the continental sources of terrigeneous sediment for the CDW and AABW compared the present day, and the NADW is still unable to transport sediments from the Scotia Sea. Consequently, it excludes the NADW as a transport medium for the cohesive silt mode fraction to site MD07-3076Q. Therefore, because the NADW is also the only water-mass able to transport sediment from the South American Shield to our study site, it excludes the South American Shield as a source of sediment for the cohesive silt mode fraction, and implies East Antarctica as the source of old material identified in the cohesive silt mode fraction. The terrigenous supplies deriving from East Antarctica/Scotia Sea strongly suggest the AABW has been the dominant carrier of the 2–20 μm grain-size fraction since the LGM. In addition, because the mean isotopic composition of this grain-size fraction transported by the AABW is relatively constant through time (Fig. 6), the relative contributions of East Antarctica and Scotia Sea area seem to have remained largely unchanged since the LGM.

5.2.3. Sortable silt mode fraction (20–32/40 μm): A LCDW signal

A part of the particles transported by the AABW and the NADW are derived from old crustal sources (i.e., East Antarctica and South American Shield, respectively). Thence, these two deep-water masses cannot be the source of the sortable silt mode fraction during the LGM. In contrast, the CDW is a good candidate to transport particles solely from the Scotia Sea, as identified for the sortable silt mode fraction during the LGM. Consequently, the only possible source of this grain size fraction is the CDW. During the deglaciation, the Nd isotope composition of the sortable silt mode fraction became gradually less radiogenic while the $^{87}Sr/^{86}Sr$ ratio fluctuated, suggesting a modification of provenances and/or an additional contribution of less radiogenic Nd source. Such isotopic changes could be explained in two ways; (1) a change in the CDW pathway; (2) the incorporation of terrigenous material by mixing with other water-masses (such as AABW or NADW). The CDW slowed down and migrated southward during the deglaciation in concert with the southward migration of the subpolar and polar fronts (Howard and Prell, 1992; Anderson et al., 2009; Denton et al., 2010). However, such a change in the CDW pathway would have no effect on the terrigenous sources of particles. In contrast, several studies proposed increased ventilation in the Southern Ocean, enabling the degassing of oceanic CO_2 to the atmosphere (Ahn and Brook, 2008; Fischer et al., 2010; Skinner et al., 2010, 2013; 2014; Siani et al., 2013). Currently the base of the LCDW is mixed with the AABW, which was apparently not the case during the LGM (Skinner et al., 2010). The onset of AABW/LCDM mixing could explain the incorporation of unradiogenic terrigenous material from the Weddell Sea embayment (i.e., East Antarctica) into the LCDW. This mechanism likely explains the shift in ε_{Nd} composition during the deglaciation. This hypothesis is supported by the results of Walter et al. (2000) who reported lower ε_{Nd} in terrigenous sediments in the southern Scotia Sea during the interglacial period and interpreted this as higher contribution of sediment from the Weddell Sea embayment due to the mixing of the AABW into the ACC. From 15 ka, the Nd isotope composition of the sortable silt mode fraction is very close to the one from the cohesive silt mode fraction transported by the AABW. It suggests that the sortable silt mode fraction is specifically transported by the LCDW rather than by the entire CDW. This highlights the fact that the ε_{Nd} variations from the sortable silt mode fraction provide a useful tool to study the mixing between the AABW and LCDW.

6. Paleoceanographic implication

Our results establish that different grain-size modes can be attributed to distinct water-masses and that variation of the particle size of the different grain-size modes (Fig. 2) can be used to record the variations of flow speed of these water-masses as well as changes in pathways/mixing. This method has the advantage of distinguishing the speed of each water mass instead of giving the average speed of all the water masses, as it is the case for the sortable silt method (McCave and Hall, 2006). During the last glacial period, the large mean particle diameter (>30 μm) of the sortable silt mode fraction reflects strong LCDW activity. At the beginning of the deglaciation, the variation of the mean particle size suggests that the LCDW speed slightly decreased, but remained high. Since ~15 ka, the LCDW speed has been showing a gradual decrease. McCave et al. (2014) observed minor change in the Antarctic Circumpolar Current (which includes the CDW) flow speed at the Drake Passage during the deglaciation. Our observation, however, is consistent with other studies in the south Indian sector of the Southern Ocean indicating that the Antarctic Circumpolar Current (which includes the CDW) flow speed was maximum during the LGM and decreased during the deglaciation (Mazaud et al., 2010), with a notable increase from ~15 ka on (Mazaud et al., in prep.). Altogether, these studies and our results suggest that the weakening of the ACC started at ~15 ka.

From ~26 to 21 ka, the low particle sizes recorded in the cohesive silt mode (Fig. 2 b, transported by the AABW) indicate slow AABW, which is consistent with the observed moderate relative contribution of AABW in clay particles (Figs. 8 and 9). In this time interval, one isolated high value is recorded at 24 ka and suggests that, temporarily, AABW activity was stronger. However, no change is registered in the clay minerals (Figs. 3 and 9). The grain-size data indicate that the AABW became more vigorous from 21 ka to reach its strongest speed at the end of the LGM. This maximum speed is concomitant with the strongest relative contribution of the AABW of the clay record (Fig. 3h and 9), as shown by the peak of the illite/smectite ratio (Fig. 3) illustrated on Fig. 8. Interestingly, this AABW maximum preceded the HS 1, and both its speed and relative contribution fell at the LGM/HS 1 transition as defined by Missiaen et al. (2019). At the beginning of the deglaciation, the abrupt decrease of the fine grain-size mode indicates a slowdown of the AABW (Fig. 2). This is supported by a sharp decrease in the illite/smectite ratio in the clay-size fraction (Fig. 3), which also suggests an abrupt decrease of the relative contribution of the AABW. At ~16 ka, a slowdown of the AABW is indicated by a second sharp decrease of the cohesive silt mode (Fig. 2), which reaches its lowest values of the entire record, indicating low AABW speed from 16 to 11.5 ka, when the AABW activity increased suddenly and recovered

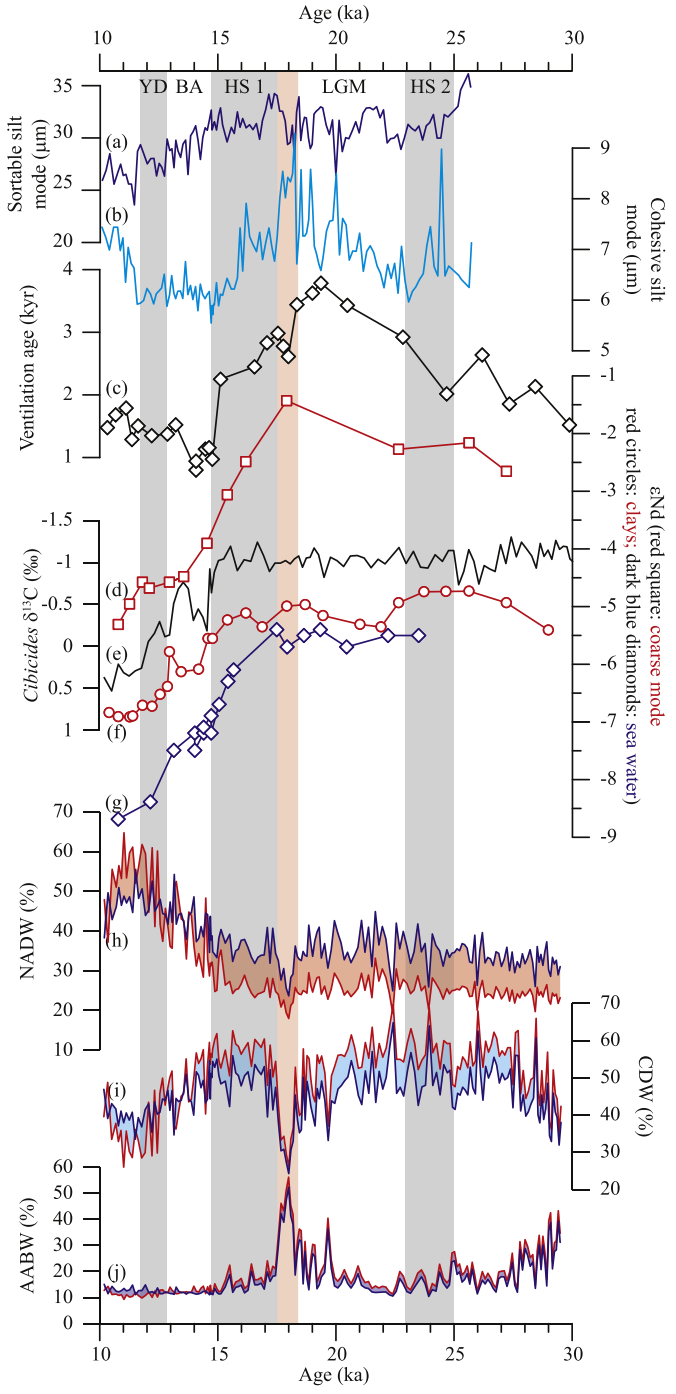

Fig. 9. Comparison between paleoceanographic proxies from core MD07-3076Q and data produced in this study. Grey areas delimit the main climatic events and the red band highlights the particularly strong AABW event. (a) size of the sortable silt mode (μm), a proxy of the speed of the LCDW; (b) size of the cohesive silt mode (μm), a proxy of the speed of the AABW; (c) bottom water ventilation age from site MD07-3076Q (data from Skinner et al., 2010); (d) ε_{Nd} from the sortable silt size fraction; (e) Cibicides $\delta^{13}C$ from site MD07-3076Q (Waelbroeck et al., 2011); (f) ε_{Nd} from the cohesive silt size fraction; (g) seawater ε_{Nd} from site MD07-3076Q (Skinner et al., 2013); (h) proportion of clay particles delivered by the NADW (see Fig. 8b); (i) proportion of clay particles delivered by the CDW (see Fig. 8b); (j) proportion of clay particles delivered by the AABW (see Fig. 8b). On curves (h), (i) and (j), the red line represent values calculated using the Holocene end-member of the NADW (I/S = 0.5), while the blue line correspond to the values calculated using the LGM end-member of the NADW (I/S = 1). (For interpretation of the references to colour in this figure legend, the reader is referred to the Web version of this article.)

the speed observed before 16 ka.

These variations of the AABW speed could indicate the transition from the Ice Shelf Mode dominated bottom water formation at the end of the LGM to the Polynyas Mode dominated bottom water formation during interglacial periods. The variations of the cohesive silt mode support a strong AABW during the LGM and the early Holocene, and a minimum flow during the deglaciation. This minimum flow would result from the reduction of bottom water production via the Ice Shelf Mode and still low production via the Polynyas Mode. Our results confirm the results of Krueger et al. (2012) who demonstrated the relation between the flow speed changes in the Cape Basin and the higher AABW production rates and indicate that the size of the cohesive silt mode is a reliable tracer of the AABW flow speed and hence of AABW production rates in the Weddell Sea.

Overall, the variations of the AABW flow speed and ventilation age are similar, with higher average speeds corresponding to the old ventilation ages. Taken together with the reconstructed vigorous LCDW during the LGM (Fig. 9 a.), these observations suggest that the deep Southern Ocean was poorly ventilated but with a vigorous circulation. It means that both the AABW and LCDW remained isolated from the surface during the LGM. This conclusion is consistent with our hypothesis that AABW was formed under ice shelves during this period and that the major expansion of sea ice (Bianchi and Gersonde, 2004; Bostock et al., 2013; Adkins, 2013) kept the AABW isolated from the atmosphere during the LGM. In addition, poorly ventilated deep Southern Ocean associated with a vigorous deep circulation (i.e., high AABW and LCDW flow) suggests that a barrier existed between the deep ocean and the surface, which is consistent with the study of Howe et al. (2016). In contrast, direct comparison highlights the fact that the peaks of ventilation age and of the AABW flow are not in phase. Indeed, the peaks of the AABW flow (Fig. 9b) and of the AABW contribution to clay deposition (Fig. 9j) are synchronous with the first decrease in deep water ventilation ages after the LGM and prior to HS1. Moreover, this well-defined change in the AABW behavior is recorded by two distinct proxies (i.e., clay minerals and grain size distribution) and in two distinct grain size fractions (clays and silts). These synchronous changes are associated with a drop in ventilation age prior to the HS 1. The variations in two grain size fractions that are transported and deposited by distinct dynamic processes indicates a major perturbation in Southern Ocean circulation. Interestingly, the increase in the AABW strength associated to the early decrease in deep water ventilation age took place significantly earlier than the changes recorded by the other proxies measured in core MD07-3076Q (i.e., sea water ε_{Nd} between 17.5 and 16 ka, $\delta^{13}C$ at 14.5 ka, $\delta^{18}O$ at 15 ka, LCDW flow speed at 15 ka, NADW proportion at 15 ka) and also precedes the atmospheric CO_2 rise (Bereiter et al., 2015) and the change in the opal flux (Anderson et al., 2009). For the first time, these data indicate a change in the deep Southern Ocean circulation that is associated with ventilation change that precedes the HS 1. This suggest that the identified large temporary (~1 kyr long) increase in the AABW contribution and flow speed may have had a substantial impact on the deep Southern Ocean ventilation, and by extension, on the deglacial CO_2 rise. Indeed, the magnitude of the change in the AABW behavior has the potential to "break" the hypothetical physical barrier between the deep Southern Ocean and the surface that was responsible of poorly ventilated deep water during the LGM. This combination of events also explains the unexpected early fall of the deep water ventilation age observed at ~18.2 ka.

7. Conclusion

The mineralogical characteristics of the clay-size fraction

provide new insights into the general thermohaline circulation in the southern South Atlantic. The mineralogical signal demonstrates strong influence of both the CDW and AABW during the last glacial period. Clay assemblages reveal a particularly high contribution of the AABW at the end of the LGM, which is interpreted as reflecting strong Ice Shelf Mode bottom water production in the Weddell Sea. The contribution of the CDW and AABW then progressively decreases during the deglaciation together with the growing influence of the NADW (Fig. 8). Indeed, clay size fraction data monitor the progressive incursion of NADW into the Southern Ocean during the deglaciation from ~15 ka (Fig. 8), as well as the synchronous southward retreat of the southern-born deep water-masses (i.e., CDW and AABW).

The isotopic compositions of the distinct grain size modes provides invaluable information. The sortable silt mode fraction helps to trace the LCDW activity whereas the cohesive silt mode fraction is associated with the AABW signal. Consequently, the temporal evolution of flow speeds, pathways and interactions of these deep water-masses can be determined in a very robust way. This study suggests: (1) vigorous LCDW during the LGM and a marked weakening from ~15 ka; (2) strong AABW at the end of the LGM and during the early Holocene, and weak AABW during the deglaciation between 16 and 11.5 ka. These results suggest a decrease of AABW production rates during the deglaciation that could result from the transition from strong Ice Shelf Mode bottom water production during the LGM to stronger Polynyas Mode bottom water during the Holocene.

The strong LCDW speed observed during the LGM is associated with increased clay deposition by the CDW, and the reduction of LCDW speed since the B/A is accompanied by an increased clay contribution from the NADW. Similarly, the highest AABW speed recorded at the end of the LGM is concomitant with the highest relative contribution of the AABW to clay mineral deposition. Interestingly, this AABW maximum preceded the HS 1 and both its speed and contribution fell markedly at the LGM/HS 1 transition.

Finally, this study demonstrates that based on (1) the combination of isotopic and mineral investigation of the clay size fraction, (2) the combination of isotopic measurement of isolated grain size modes and of grain size distribution results, and (3) a complete synthesis of the potential sources of sediments, it is possible to obtain reliable information on the lithogenic material transported by each deep water mass. This approach allows efficient tracking of the evolution of distinct water-masses through time, since it helps to isolate the specific signal associated to each water-mass. Based on these observations, we conclude that the increase in the AABW strength at the end of the LGM may have had a substantial impact on the ventilation recovery of the deep Southern Ocean, and by extension, to the deglacial CO_2 rise.

Acknowledgments

We wish to thank Richard Smeets for his invaluable help in the clean lab, Emmeke Bos, Janne Koorneef, and Mathijs van de Ven for the help with TIMS Triton measurements, Bas van der Wagt and Kirsten van Zuilen for Neptune MC-ICPMS measurements. Tristan Lippens is thanked for computer support. We also wish to thank all organizations that provided financial support to the project: the “region Haut de France” and the Vrije Universiteit of Amsterdam. The research was supported by Europlanet 2020 RI, which received funding from the European Union’s Horizon 2020 research and innovation programme under grant agreement No 654208. We also want to express our special thanks to the “flotte océanographique française” for retrieving the sediment core used in this study. FB and VBR thanks Monique Gentric for administrative support. CW acknowledges support from the European Research Council ERC grant ACCLIMATE/n° 339108.

Appendix A. Supplementary data

Supplementary data to this article can be found online at https://doi.org/10.1016/j.quascirev.2019.106089.

References

Adkins, J.F., 2013. The role of deep ocean circulation in setting glacial climates. Paleoceanography 28, 539–561. https://doi.org/10.1002/palo.20046, 2013.
Ahn, J., Brook, E.J., 2008. Atmospheric CO2 and climate on millennial time scales during the last glacial period. Science 322, 83. https://doi.org/10.1126/science.1160832.
Allègre, C.J., Dupré, B., Négrel, P., Gaillardet, J., 1996. Sr-Nd-Pb isotope systematics in Amazon and Congo River systems: constraints about erosion processes. Chem. Geol. 131, 93–112. https://doi.org/10.1016/0009-2541(96)00028-9.
Anderson, J.J., 1965. Bedrock geology of Antarctica: a summary of exploration, 1831–1962. Geol. Paleontol. Antarct. 6, 1–70. https://doi.org/10.1029/AR006p0001.
Anderson, R.F., Ali, S., Bradtmiller, L.I., Nielsen, S.H.H., Fleisher, M.Q., Anderson, B.E., Burckle, L.H., 2009. Wind-driven upwelling in the Southern Ocean and the deglacial rise in atmospheric CO2. Science 323, 1443. https://doi.org/10.1126/science.1167441.
Barker, S., Diz, P., Vautravers, M.J., Pike, J., Knorr, G., Hall, I.R., Broecker, W.S., 2009. Interhemispheric Atlantic seesaw response during the last deglaciation. Nature 457, 1097. https://doi.org/10.1038/nature07770.
Barker, S., Knorr, G., Vautravers, M.J., Diz, P., Skinner, L.C., 2010. Extreme deepening of the Atlantic overturning circulation during deglaciation. Nat. Geosci. 3, 567. https://doi.org/10.1038/ngeo921.
Barreiro, B., 1983. Lead isotopic compositions of South Sandwich Island volcanic rocks and their bearing on magmagenesis in intra-oceanic island arcs. Geochem. Cosmochim. Acta 47, 817–822. https://doi.org/10.1016/0016-7037(83)90115-1.
Barrett, P.J., 1991. The devonian to Jurassic Beacon supergroup of the Transantarctic mountains and correlatives in other parts of Antarctica. The Geology of Antarctica, pp. 120–152.
Barros, A.M., Silva, R.D., Cardoso, O.R.F.A., Freire, F.A., Souza Junior, J.J., Rivetti, M., Luz, D.S., Palmeira, R.C.B., Tassinari, C.C.G., 1982. Geologia, BRASIL. Ministério das Minas e Energia. Projeto RADAMBRASIL Folha SD.
Basile, I., Grousset, F.E., Revel, M., Petit, J.R., Biscaye, P.E., Barkov, N.I., 1997. Patagonian origin of glacial dust deposited in East Antarctica (Vostok and Dome C) during glacial stages 2, 4 and 6. Earth Planet. Sci. Lett. 146, 573–589. https://doi.org/10.1016/S0012-821X(96)00255-5.
Bayon, G., Burton, K.W., Soulet, G., Vigier, N., Dennielou, B., Etoubleau, J., Ponzevera, E., German, C.R., Nesbitt, R.W., 2009. Hf and Nd isotopes in marine sediments: constraints on global silicate weathering. Earth Planet. Sci. Lett. 277, 318–326. https://doi.org/10.1016/j.epsl.2008.10.028.
Bayon, G., Skonieczny, C., Delvigne, C., Toucanne, S., Bermell, S., Ponzevera, E., André, L., 2016. Environmental Hf–Nd isotopic decoupling in World river clays. Earth Planet. Sci. Lett. 438, 25–36. https://doi.org/10.1016/j.epsl.2016.01.010.
Bayon, G., Toucanne, S., Skonieczny, C., André, L., Bermell, S., Cheron, S., Dennielou, B., Etoubleau, J., Freslon, N., Gauchery, T., Germain, Y., Jorry, S.J., Ménot, G., Monin, L., Ponzevera, E., Rouget, M.-L., Tachikawa, K., Barrat, J.A., 2015. Rare earth elements and neodymium isotopes in world river sediments revisited. Geochem. Cosmochim. Acta 170, 17–38. https://doi.org/10.1016/j.gca.2015.08.001.
Beny, F., Toucanne, S., Skonieczny, C., Bayon, G., Ziegler, M., 2018. Geochemical provenance of sediments from the northern East China Sea document a gradual migration of the Asian Monsoon belt over the past 400,000 years. Quat. Sci. Rev. 190, 161–175. https://doi.org/10.1016/j.quascirev.2018.04.032.
Bereiter, B., Eggleston, S., Schmitt, J., Nehrbass-Ahles, C., Stocker, T.F., Fischer, H., Kipfstuhl, S., Chappellaz, J., 2015. Revision of the EPICA Dome C CO2 record from 800 to 600 kyr before present. Geophys. Res. Lett. 42, 542–549. https://doi.org/10.1002/2014GL061957.
Bianchi, C., Gersonde, R., 2004. Climate evolution at the last deglaciation: the role of the Southern Ocean. Earth Planet. Sci. Lett. 228, 407–424. https://doi.org/10.1016/j.epsl.2004.10.003.
Bostock, H.C., Barrows, T.T., Carter, L., Chase, Z., Cortese, G., Dunbar, G.B., Ellwood, M., Hayward, B., Howard, W., Neil, H.L., Noble, T.L., Mackintosh, A., Moss, P.T., Moy, A.D., White, D., Williams, M.J.M., Armand, L.K., 2013. A review of the Australian–New Zealand sector of the Southern Ocean over the last 30 ka (Aus-INTIMATE project). Quat. Sci. Rev. 74, 35–57. https://doi.org/10.1016/j.quascirev.2012.07.018.
Bouttes, N., Paillard, D., Roche, D.M., Waelbroeck, C., Kageyama, M., Lourantou, A., Michel, E., Bopp, L., 2012. Impact of oceanic processes on the carbon cycle during the last termination. Clim. Past 8, 149–170. https://doi.org/10.5194/CP-8-149-2012.
Bremner, J.M., Willis, J.P., 1993. Mineralogy and geochemistry of the clay fraction of sediments from the Namibian continental margin and the adjacent hinterland. Mar. Geol. 115, 85–116. https://doi.org/10.1016/0025-3227(93)90076-8.
Brown, G., 1980. X-ray Diffraction Procedures for Clay Mineral Identification. Crystal

structures of clay minerals and their X-ray identification, pp. 305–359.
Burke, A., Robinson, L.F., 2012. The Southern Ocean's role in carbon exchange during the last deglaciation. Science 335, 557–561. https://doi.org/10.1126/science.1208163.
Campodonico, V.A., García, M.G., Pasquini, A.I., 2016. The geochemical signature of suspended sediments in the Parana River basin: implications for provenance, weathering and sedimentary recycling. Catena 143, 201–214. https://doi.org/10.1016/j.catena.2016.04.008.
Capurro, L.R., 1955. Expedición argentina al Mar de Weddell, diciembre de 1954 a enero de 1955. República Argentina. Ministerio de Marina, Dirección General de Navegación.
Clapperton, C.M., 1993. Quaternary Geology and Geomorphology of South America. Elsevier Amsterdam etc.
Cohen, R.S., O'Nions, R.K., 1982. Identification of recycled continental material in the mantle from Sr, Nd and Pb isotope investigations. Earth Planet. Sci. Lett. 61, 73–84. https://doi.org/10.1016/0012-821X(82)90040-1.
Cordani, U.G., Sato, K., 1999. Crustal evolution of the South American Platform, based on Nd isotopic systematics on granitoid rocks. Episodes-Newsmag. Int. Union Geol. Sci. 22, 167–173.
Curry, W.B., Oppo, D.W., 2005. Glacial water mass geometry and the distribution of δ13C of ΣCO2 in the western Atlantic Ocean. Paleoceanography 20. https://doi.org/10.1029/2004PA001021.
de Alkmim, F.F., 2015. Geological background: a tectonic Panorama of Brazil. In: Vieira, B.C., Salgado, A.A.R., Santos, L.J.C. (Eds.), Landscapes and Landforms of Brazil. Springer Netherlands, Dordrecht, pp. 9–17. https://doi.org/10.1007/978-94-017-8023-0_2.
de Almeida, F.F.M., Hasui, Y., de Brito Neves, B.B., Fuck, R.A., 1981. Brazilian structural provinces: an introduction. Earth Sci. Rev. 17, 1–29. https://doi.org/10.1016/0012-8252(81)90003-9.
de Mahiques, M.M., Tassinari, C.C.G., Marcolini, S., Violante, R.A., Figueira, R.C.L., da Silveira, I.C.A., Burone, L., de Mello e Sousa, S.H., 2008. Nd and Pb isotope signatures on the Southeastern South American upper margin: implications for sediment transport and source rocks. Mar. Geol. 250, 51–63. https://doi.org/10.1016/j.margeo.2007.11.007.
D'el-Rey Silva, L.J.H., Walde, D.H.-G., Saldanha, D.O., 2016. The Neoproterozoic–Cambrian Paraguay Belt, central Brazil: Part I — new structural data and a new approach on the regional implications. Tectonophysics 676, 20–41. https://doi.org/10.1016/j.tecto.2016.03.019.
Denton, G.H., Anderson, R.F., Toggweiler, J.R., Edwards, R.L., Schaefer, J.M., Putnam, A.E., 2010. The last glacial termination. Science 328, 1652. https://doi.org/10.1126/science.1184119.
DePaolo, D.J., Manton, W.I., Grew, E.S., Halpern, M., 1982. Sm–Nd, Rb–Sr and U–Th–Pb systematics of granulite facies rocks from Fyfe Hills, Enderby Land, Antarctica. Nature 298, 614–618. https://doi.org/10.1038/298614a0.
Desiage, P.-A., Montero-Serrano, J.-C., St-Onge, G., Crespi-Abril, A.C., Giarratano, E., Gil, M.N., Haller, M.J., 2018. Quantifying sources and transport pathways of surface sediments in the Gulf of San Jorge, central Patagonia (Argentina). Oceanography 31, 92–103.
Dezileau, L., Bareille, G., Reyss, J.L., Lemoine, F., 2000. Evidence for strong sediment redistribution by bottom currents along the southeast Indian ridge. Deep Sea Res. Oceanogr. Res. Pap. 47, 1899–1936. https://doi.org/10.1016/S0967-0637(00)00008-X.
Diekmann, B., 2007. Sedimentary patterns in the late quaternary Southern Ocean. Deep Sea Res. Part II Top. Stud. Oceanogr. 54, 2350–2366. https://doi.org/10.1016/j.dsr2.2007.07.025.
Diekmann, B., Kuhn, G., Rachold, V., Abelmann, A., Brathauer, U., Fütterer, D.K., Gersonde, R., Grobe, H., 2000. Terrigenous sediment supply in the Scotia sea (Southern Ocean): response to late quaternary ice dynamics in Patagonia and on the Antarctic Peninsula. Palaeogeogr. Palaeoclimatol. Palaeoecol. 162, 357–387. https://doi.org/10.1016/S0031-0182(00)00138-3.
Engler, A., 2009. The geology of south America. In: Geology. Encyclopedia of Life Support Systems, p. 11.
Esquevin, J., 1969. Influence de la composition chimique des illites sur leur cristallinité. Bull. Centre Rech. Pau-SNPA 3, 147–153.
Fischer, H., Schmitt, J., Lüthi, D., Stocker, T.F., Tschumi, T., Parekh, P., Joos, F., Köhler, P., Völker, C., Gersonde, R., Barbante, C., Le Floch, M., Raynaud, D., Wolff, E., 2010. The role of Southern Ocean processes in orbital and millennial CO2 variations – a synthesis. Quat. Sci. Rev. 29, 193–205. https://doi.org/10.1016/j.quascirev.2009.06.007.
Flowerdew, M.J., Tyrrell, S., Riley, T.R., Whitehouse, M.J., Mulvaney, R., Leat, P.T., Marschall, H.R., 2012. Distinguishing East and West Antarctic sediment sources using the Pb isotope composition of detrital K-feldspar. Chem. Geol. 292–293, 88–102. https://doi.org/10.1016/j.chemgeo.2011.11.006.
Foster, T.D., Carmack, E.C., 1976. Frontal zone mixing and Antarctic Bottom water formation in the southern Weddell Sea. Deep Sea Res. Oceanogr. Abstr. 23, 301–317. https://doi.org/10.1016/0011-7471(76)90872-X.
Fretzdorff, S., Livermore, R.A., Devey, C.W., Leat, P.T., Stoffers, P., 2002. Petrogenesis of the back-arc east scotia ridge, south Atlantic ocean. J. Petrol. 43, 1435–1467. https://doi.org/10.1093/petrology/43.8.1435.
Fuck, R.A., Dantas, E.L., Pimentel, M.M., Botelho, N.F., Armstrong, R., Laux, J.H., Junges, S.L., Soares, J.E., Praxedes, I.F., 2014. Paleoproterozoic crust-formation and reworking events in the Tocantins Province, central Brazil: a contribution for Atlantica supercontinent reconstruction. Precambrian Res. 244, 53–74. https://doi.org/10.1016/j.precamres.2013.12.003.
Ganade de Araujo, C.E., Cordani, U.G., Weinberg, R.F., Basei, M.A.S., Armstrong, R., Sato, K., 2014. Tracing Neoproterozoic subduction in the Borborema Province (NE-Brazil): clues from U-Pb geochronology and Sr-Nd-Hf-O isotopes on granitoids and migmatites. Lithos 202–203, 167–189. https://doi.org/10.1016/j.lithos.2014.05.015.
Gersonde, R., Abelmann, A., Brathauer, U., Becquey, S., Bianchi, C., Cortese, G., Grobe, H., Kuhn, G., Niebler, H.-S., Segl, M., Sieger, R., Zielinski, U., Fütterer, D.K., 2003. Last glacial sea surface temperatures and sea-ice extent in the Southern Ocean (Atlantic-Indian sector): a multiproxy approach. Paleoceanography 18. https://doi.org/10.1029/2002PA000809.
Gherardi, J.-M., Labeyrie, L., Nave, S., Francois, R., McManus, J.F., Cortijo, E., 2009. Glacial-interglacial circulation changes inferred from 231Pa/230Th sedimentary record in the North Atlantic region. Paleoceanography 24. https://doi.org/10.1029/2008PA001696.
Gottschalk, J., Skinner, L.C., Lippold, J., Vogel, H., Frank, N., Jaccard, S.L., Waelbroeck, C., 2016. Biological and physical controls in the Southern Ocean on past millennial-scale atmospheric CO2 changes. Nat. Commun. 7, 11539. https://doi.org/10.1038/ncomms11539.
Gottschalk, J., Skinner, L.C., Misra, S., Waelbroeck, C., Menviel, L., Timmermann, A., 2015a. Abrupt changes in the southern extent of north Atlantic deep water during dansgaard–Oeschger events. Nat. Geosci. 8, 950. https://doi.org/10.1038/NGEO2558.
Gottschalk, J., Skinner, L.C., Waelbroeck, C., 2015b. Contribution of seasonal sub-Antarctic surface water variability to millennial-scale changes in atmospheric CO2 over the last deglaciation and Marine Isotope Stage 3. Earth Planet. Sci. Lett. 411, 87–99. https://doi.org/10.1016/j.epsl.2014.11.051.
Govin, A., Michel, E., Labeyrie, L., Waelbroeck, C., Dewilde, F., Jansen, E., 2009. Evidence for northward expansion of Antarctic Bottom Water mass in the Southern Ocean during the last glacial inception. Paleoceanography 24. https://doi.org/10.1029/2008PA001603.
Grousset, F.E., Rognon, P., Coudé-Gaussen, G., Pédemay, P., 1992. Origins of peri-Saharan dust deposits traced by their Nd and Sr isotopic composition. Palaeogeogr. Palaeoclimatol. Palaeoecol. 93, 203–212. https://doi.org/10.1016/0031-0182(92)90097-O.
Guyot, J.L., Jouanneau, J.M., Soares, L., Boaventura, G.R., Maillet, N., Lagane, C., 2007. Clay mineral composition of river sediments in the Amazon Basin. Catena 71, 340–356. https://doi.org/10.1016/j.catena.2007.02.002.
Hall, I.R., McCave, I.N., Shackleton, N.J., Weedon, G.P., Harris, S.E., 2001. Intensified deep Pacific inflow and ventilation in Pleistocene glacial times. Nature 412, 809–812. https://doi.org/10.1038/35090552.
Harrison, D., Leat, P.T., Burnard, P.G., Turner, G., Fretzdorff, S., Millar, I.L., 2003. Resolving mantle components in oceanic lavas from segment E2 of the East Scotia back-arc ridge, South Sandwich Islands. Geol. Soc. Lond. Spec. Publ. 219, 333. https://doi.org/10.1144/GSL.SP.2003.219.01.16.
Hauptvogel, D.W., Passchier, S., 2012. Early–Middle Miocene (17–14Ma) Antarctic ice dynamics reconstructed from the heavy mineral provenance in the AND-2A drill core, Ross Sea, Antarctica. Glob. Planet. Chang. 82 (83), 38–50. https://doi.org/10.1016/j.gloplacha.2011.11.003.
Hegner, E., Dauelsberg, H.J., Rutgers Van Der Loeff, M.M., Jeandel, C., De Baar, H.J.W., 2007. Nd isotopic constraints on the origin of suspended particles in the Atlantic Sector of the Southern Ocean. Geochem. Geophys. Geosyst. 8 https://doi.org/10.1029/2007GC001666.
Hole, M.J., Kempton, P.D., Millar, I.L., 1993. Trace-element and isotopic characteristics of small-degree melts of the asthenosphere: evidence from the alkalic basalts of the Antarctic Peninsula. Chem. Geol. 109, 51–68. https://doi.org/10.1016/0009-2541(93)90061-M.
Howard, W.R., Prell, W.L., 1992. Late quaternary surface circulation of the southern Indian ocean and its relationship to orbital variations. Paleoceanography 7, 79–117. https://doi.org/10.1029/91PA02994.
Howe, J.N.W., Piotrowski, A.M., Noble, T.L., Mulitza, S., Chiessi, C.M., Bayon, G., 2016. North Atlantic deep water production during the last glacial maximum. Nat. Commun. 7, 11765. https://doi.org/10.1038/ncomms11765.
Jaccard, S.L., Hayes, C.T., Martínez-García, A., Hodell, D.A., Anderson, R.F., Sigman, D.M., Haug, G.H., 2013. Two modes of change in Southern Ocean productivity over the past million years. Science 339, 1419. https://doi.org/10.1126/science.1227545.
Jeandel, C., Arsouze, T., Lacan, F., Téchiné, P., Dutay, J.-C., 2007. Isotopic Nd compositions and concentrations of the lithogenic inputs into the ocean: a compilation, with an emphasis on the margins. Chem. Geol. 239, 156–164. https://doi.org/10.1016/j.chemgeo.2006.11.013.
Khondoker, R., Weiss, D., van de Flierdt, T., Rehkämper, M., Kreissig, K., Coles, B.J., Strekopytov, S., Humphreys-Williams, E., Dong, S., Bory, A., Bout-Roumazeilles, V., Smichowski, P., Cid-Agüero, P., Babinski, M., Losno, R., Monna, F., 2018. New constraints on elemental and Pb and Nd isotope compositions of south American and southern African aerosol sources to the south Atlantic Ocean. Geochemistry 78, 372–384. https://doi.org/10.1016/j.chemer.2018.05.001.
Köhler, P., Fischer, H., 2006. Simulating low frequency changes in atmospheric CO2 during the last 740 000 years. Clim. Past 2, 57–78.
Košler, J., Magna, T., Mlčoch, B., Mixa, P., Nývlt, D., Holub, F.V., 2009. Combined Sr, Nd, Pb and Li isotope geochemistry of alkaline lavas from northern James Ross Island (Antarctic Peninsula) and implications for back-arc magma formation. Chem. Geol. 258, 207–218. https://doi.org/10.1016/j.chemgeo.2008.10.006.
Krueger, S., Leuschner, D.C., Ehrmann, W., Schmiedl, G., Mackensen, A., 2012. North Atlantic deep water and Antarctic bottom water variability during the last 200ka recorded in an abyssal sediment core off South Africa. Glob. Planet.

Chang. 80 (81), 180–189. https://doi.org/10.1016/j.gloplacha.2011.10.001.
Krueger, S., Leuschner, D.C., Ehrmann, W., Schmiedl, G., Mackensen, A., Diekmann, B., 2008. Ocean circulation patterns and dust supply into the South Atlantic during the last glacial cycle revealed by statistical analysis of kaolinite/chlorite ratios. Mar. Geol. 253, 82–91. https://doi.org/10.1016/j.margeo.2008.04.015.
Kuhn, G., Diekmann, B., 2002. Late Quaternary variability of ocean circulation in the southeastern South Atlantic inferred from the terrigenous sediment record of a drift deposit in the southern Cape Basin (ODP Site 1089). Palaeogeogr. Palaeoclimatol. Palaeoecol. 182, 287–303. https://doi.org/10.1016/S0031-0182(01)00500-4.
Laird, M.G., 1991. The late Proterozoic-middle Palaeozoic rocks of Antarctica. In: The Geology of Antarctica, pp. 74–119.
Lambert, F., Delmonte, B., Petit, J.R., Bigler, M., Kaufmann, P.R., Hutterli, M.A., Stocker, T.F., Ruth, U., Steffensen, J.P., Maggi, V., 2008. Dust-climate couplings over the past 800,000 years from the EPICA Dome C ice core. Nature 452, 616. https://doi.org/10.1038/nature06763.
Larqué, L., Maamaatuaiahutapu, K., Garçon, V., 1997. On the intermediate and deep water flows in the South Atlantic Ocean. J. Geophys. Res.: Oceans 102, 12425–12440.
Le Quéré, C., Rödenbeck, C., Buitenhuis, E.T., Conway, T.J., Langenfelds, R., Gomez, A., Labuschagne, C., Ramonet, M., Nakazawa, T., Metzl, N., Gillett, N., Heimann, M., 2007. Saturation of the Southern Ocean CO2 sink due to recent climate change. Science 316, 1735. https://doi.org/10.1126/science.1136188.
Lee, J.I., Park, B.-K., Jwa, Y.-J., Ho Il, Yoon, Kyu Chul, Yoo, Kim, Y., 2005. Geochemical characteristics and the provenance of sediments in the Bransfield strait, west Antarctica. Mar. Geol. 219, 81–98. https://doi.org/10.1016/j.margeo.2005.06.002.
Luttinen, A.V., Leat, P.T., Furnes, H., 2010. Björnnutane and Sembberget basalt lavas and the geochemical provinciality of Karoo magmatism in western Dronning Maud Land, Antarctica. J. Volcanol. Geotherm. Res. 198, 1–18. https://doi.org/10.1016/j.jvolgeores.2010.07.011.
Luttinen, A.V., Rämö, O.T., Huhma, H., 1998. Neodymium and strontium isotopic and trace element composition of a Mesozoic CFB suite from Dronning Maud Land, Antarctica: implications for lithosphere and asthenosphere contributions to Karoo magmatism. Geochem. Cosmochim. Acta 62, 2701–2714. https://doi.org/10.1016/S0016-7037(98)00184-7.
Mallmann, G., Chemale, F., Ávila, J.N., Kawashita, K., Armstrong, R.A., 2007. Isotope geochemistry and geochronology of the Nico Pérez Terrane, Rio de la Plata craton, Uruguay. Gondwana Res. 12, 489–508. https://doi.org/10.1016/j.gr.2007.01.002.
Martínez-García, A., Sigman, D.M., Ren, H., Anderson, R.F., Straub, M., Hodell, D.A., Jaccard, S.L., Eglinton, T.I., Haug, G.H., 2014. Iron fertilization of the subantarctic Ocean during the last ice age. Science 343, 1347. https://doi.org/10.1126/science.1246848.
Mathias, G.L., Nagai, R.H., Trindade, R.I.F., de Mahiques, M.M., 2014. Magnetic fingerprint of the late Holocene inception of the Río de la Plata plume onto the southeast Brazilian shelf. Palaeogeogr. Palaeoclimatol. Palaeoecol. 415, 183–196. https://doi.org/10.1016/j.palaeo.2014.03.034.
Mazaud, A., Michel, E., Dewilde, F., Turon, J.L., 2010. Variations of the Antarctic circumpolar current intensity during the past 500 ka. Geochem. Geophys. Geosyst. 11 https://doi.org/10.1029/2010GC003033.
McCave, I.N., Andrews, J.T., 2019. Distinguishing current effects in sediments delivered to the ocean by ice. I. Principles, methods and examples. Quat. Sci. Rev. 212, 92–107. https://doi.org/10.1016/j.quascirev.2019.03.031.
McCave, I.N., Crowhurst, S.J., Kuhn, G., Hillenbrand, C.-D., Meredith, M.P., 2014. Minimal change in Antarctic Circumpolar Current flow speed between the last glacial and Holocene. Nat. Geosci. 7, 113. https://doi.org/10.1038/ngeo2037.
McCave, I.N., Hall, I.R., 2006. Size sorting in marine muds: processes, pitfalls, and prospects for paleoflow-speed proxies: size sorting IN marine muds. Geochem. Geophys. Geosyst. 7 https://doi.org/10.1029/2006GC001284 n/a-n/a.
McGee, B., Collins, A.S., Trindade, R.I.F., Jourdan, F., 2015. Investigating mid-Ediacaran glaciation and final Gondwana amalgamation using coupled sedimentology and 40Ar/39Ar detrital muscovite provenance from the Paraguay Belt, Brazil. Sedimentology 62, 130–154. https://doi.org/10.1111/sed.12143.
Menviel, L., England, M.H., Meissner, K.J., Mouchet, A., Yu, J., 2014. Atlantic-Pacific seesaw and its role in outgassing CO2 during Heinrich events. Paleoceanography 29, 58–70. https://doi.org/10.1002/2013PA002542.
Menviel, L., Joos, F., Ritz, S.P., 2012. Modeling atmospheric CO2, stable carbon isotope and marine carbon cycle changes during the last glacial-interglacial cycle. Quat. Sci. Rev. 56, 46–68.
Menviel, L., Spence, P., England, M.H., 2015a. Contribution of enhanced Antarctic Bottom Water formation to Antarctic warm events and millennial-scale atmospheric CO2 increase. Earth Planet. Sci. Lett. 413, 37–50. https://doi.org/10.1016/j.epsl.2014.12.050.
Menviel, Laurie, Spence, P., Golledge, N., England, M.H., 2015b. Southern Ocean overturning role in modulating high southern latitude climate and atmospheric CO2 on millennial timescales. Nova Acta Leopold. NF 121, 159–166.
Menviel, L., Spence, P., Yu, J., Chamberlain, M.A., Matear, R.J., Meissner, K.J., England, M.H., 2018. Southern Hemisphere westerlies as a driver of the early deglacial atmospheric CO2 rise. Nat. Commun. 9, 2503. https://doi.org/10.1038/s41467-018-04876-4.
Menviel, L., Yu, J., Joos, F., Mouchet, A., Meissner, K.J., England, M.H., 2017. Poorly ventilated deep ocean at the Last Glacial Maximum inferred from carbon isotopes: a data-model comparison study. Paleoceanography 32, 2–17. https://doi.org/10.1002/2016PA003024.
Meyer, I., Davies, G.R., Stuut, J.-B.W., 2011. Grain size control on Sr-Nd isotope provenance studies and impact on paleoclimate reconstructions: an example from deep-sea sediments offshore NW Africa. Geochem. Geophys. Geosyst. 12 https://doi.org/10.1029/2010GC003355.
Mieth, M., Jokat, W., 2014. Banded iron formation (?) at Grunehogna craton, east Antarctica – constraints from aeromagnetic data. Precambrian Res. 250, 143–150. https://doi.org/10.1016/j.precamres.2014.06.001.
Milani, E.J., Ramos, V.A., 2017. Orogenias paleozóicas no domínio sul-ocidental do Gondwana e os ciclos de subsidência da Bacia do Paraná. Rev. Bras. Geociencias 28, 473–484.
Missiaen, L., Waelbroeck, C., Pichat, S., Jaccard, S.L., Eynaud, F., Greenop, R., Burke, A., 2019. Improving North Atlantic marine core chronologies using 230Th-normalization. Paleoceanogr. Paleoclimatol. 0 https://doi.org/10.1029/2018PA003444.
Montero-Serrano, J.C., Bout-Roumazeilles, V., Sionneau, T., Tribovillard, N., Bory, A., Flower, B.P., Riboulleau, A., Martinez, P., Billy, I., 2010. Changes in precipitation regimes over North America during the Holocene as recorded by mineralogy and geochemistry of Gulf of Mexico sediments. Glob. Planet. Chang. 74, 132–143. https://doi.org/10.1016/j.gloplacha.2010.09.004.
Montero-Serrano, J.C., Bout-Roumazeilles, V., Tribovillard, N., Sionneau, T., Riboulleau, A., Bory, A., Flower, B., 2009. Sedimentary evidence of deglacial megafloods in the northern Gulf of Mexico (Pigmy Basin). Quat. Sci. Rev. 28, 3333–3347. https://doi.org/10.1016/j.quascirev.2009.09.011.
Moriarty, K.C., 1977. Clay minerals in Southeast Indian Ocean sediments, transport mechanisms and depositional environments. Mar. Geol. 25, 149–174. https://doi.org/10.1016/0025-3227(77)90051-2.
Moura, C.A., Gaudette, H., 1993. Evidence of Brasiliano/Panafrican deformation in the Araguaia belt: implication for Gondwana evolution. Rev. Bras. Geociencias 23, 117–123.
Neves, S.P., 2003. Proterozoic history of the Borborema province (NE Brazil): correlations with neighboring cratons and Pan-African belts and implications for the evolution of western Gondwana. Tectonics 22. https://doi.org/10.1029/2001TC001352.
Noble, T.L., Piotrowski, A.M., Robinson, L.F., McManus, J.F., Hillenbrand, C.-D., Bory, A.J.-M., 2012. Greater supply of Patagonian-sourced detritus and transport by the ACC to the Atlantic sector of the Southern Ocean during the last glacial period. Earth Planet. Sci. Lett. 317 (318), 374–385. https://doi.org/10.1016/j.epsl.2011.10.007.
Nogueira, A.C.R., Riccomini, C., Sial, A.N., Moura, C.A.V., Trindade, R.I.F., Fairchild, T.R., 2007. Carbon and strontium isotope fluctuations and paleoceanographic changes in the late Neoproterozoic Araras carbonate platform, southern Amazon craton, Brazil. Chem. Geol. 237, 168–190. https://doi.org/10.1016/j.chemgeo.2006.06.016.
Olivero, E.B., Martinioni, D.R., 2001. A review of the geology of the Argentinian Fuegian Andes. J. South Am. Earth Sci. Mesozoic Palaeontol. Stratigr. South Am. South Atl. 14, 175–188. https://doi.org/10.1016/S0895-9811(01)00016-5.
Orsi, A.H., Johnson, G.C., Bullister, J.L., 1999. Circulation, mixing, and production of Antarctic bottom water. Prog. Oceanogr. 43, 55–109. https://doi.org/10.1016/S0079-6611(99)00004-X.
Oyhantçabal, P., Siegesmund, S., Wemmer, K., 2011. The Río de la Plata Craton: a review of units, boundaries, ages and isotopic signature. Int. J. Earth Sci. 100, 201–220. https://doi.org/10.1007/s00531-010-0580-8.
Petit, J.R., Mourner, L., Jouzel, J., Korotkevich, Y.S., Kotlyakov, V.I., Lorius, C., 1990. Palaeoclimatological and chronological implications of the Vostok core dust record. Nature 343, 56–58.
Petschick, R., 2000. MacDiff, 4.2. 5.
Petschick, R., Kuhn, G., Gingele, F., 1996. Clay mineral distribution in surface sediments of the South Atlantic: sources, transport, and relation to oceanography. Mar. Geol. 130, 203–229. https://doi.org/10.1016/0025-3227(95)00148-4.
Pierce, E.L., Hemming, S.R., Williams, T., van de Flierdt, T., Thomson, S.N., Reiners, P.W., Gehrels, G.E., Brachfeld, S.A., Goldstein, S.L., 2014. A comparison of detrital U–Pb zircon, 40Ar/39Ar hornblende, 40Ar/39Ar biotite ages in marine sediments off East Antarctica: implications for the geology of subglacial terrains and provenance studies. Earth Sci. Rev. 138, 156–178. https://doi.org/10.1016/j.earscirev.2014.08.010.
Pimentel, M.M., Rodrigues, J.B., DellaGiustina, M.E.S., Junges, S., Matteini, M., Armstrong, R., 2011. The tectonic evolution of the Neoproterozoic Brasília Belt, central Brazil, based on SHRIMP and LA-ICPMS U–Pb sedimentary provenance data: a review. J. South Am. Earth Sci. 31, 345–357. https://doi.org/10.1016/j.jsames.2011.02.011.
Reid, J.L., 1989. On the total geostrophic circulation of the South Atlantic Ocean: flow patterns, tracers, and transports. Prog. Oceanogr. 23, 149–244. https://doi.org/10.1016/0079-6611(89)90001-3.
Roberts, J., Gottschalk, J., Skinner, L.C., Peck, V.L., Kender, S., Elderfield, H., Waelbroeck, C., Vázquez Riveiros, N., Hodell, D.A., 2016. Evolution of South Atlantic density and chemical stratification across the last deglaciation. Proc. Natl. Acad. Sci. U.S.A. 113, 514. https://doi.org/10.1073/pnas.1511252113.
Roy, M., van de Flierdt, T., Hemming, S.R., Goldstein, S.L., 2007. 40Ar/39Ar ages of hornblende grains and bulk Sm/Nd isotopes of circum-Antarctic glacio-marine sediments: implications for sediment provenance in the southern ocean. Chem. Geol. 244, 507–519. https://doi.org/10.1016/j.chemgeo.2007.07.017.
Sallée, J.B., Matear, R., Rintoul, S.R., Lenton, A., 2012. Surface to interior pathways of anthropogenic CO2 in the southern hemisphere oceans. Nat. Geosci. 5, 579–584.

Sayago, J.M., Collantes, M.M., Karlson, A., Sanabria, J., 2001. Genesis and distribution of the Late Pleistocene and Holocene loess of Argentina: a regional approximation. Quat. Int. 76 (77), 247–257. https://doi.org/10.1016/S1040-6182(00)00107-5.

Shakun, J.D., Clark, P.U., He, F., Marcott, S.A., Mix, A.C., Liu, Z., Otto-Bliesner, B., Schmittner, A., Bard, E., 2012. Global warming preceded by increasing carbon dioxide concentrations during the last deglaciation. Nature 484, 49. https://doi.org/10.1038/nature10915.

Siani, G., Michel, E., De Pol-Holz, R., DeVries, T., Lamy, F., Carel, M., Isguder, G., Dewilde, F., Lourantou, A., 2013. Carbon isotope records reveal precise timing of enhanced Southern Ocean upwelling during the last deglaciation. Nat. Commun. 4, 2758.

Siegesmund, S., Basei, M., Oyhantçabal, P., 2011. Multi-accretional tectonics at the Rio de la Plata Craton margins: preface. Int. J. Earth Sci. 100, 197–200. https://doi.org/10.1007/s00531-010-0616-0.

Skinner, L.C., Fallon, S., Waelbroeck, C., Michel, E., Barker, S., 2010. Ventilation of the deep Southern Ocean and deglacial CO2 rise. Science 328, 1147. https://doi.org/10.1126/science.1183627.

Skinner, L.C., Scrivner, A.E., Vance, D., Barker, S., Fallon, S., Waelbroeck, C., 2013. North Atlantic versus Southern Ocean contributions to a deglacial surge in deep ocean ventilation. Geology 41, 667–670. https://doi.org/10.1130/G34133.1.

Skinner, L.C., Waelbroeck, C., Scrivner, A.E., Fallon, S.J., 2014. Radiocarbon evidence for alternating northern and southern sources of ventilation of the deep Atlantic carbon pool during the last deglaciation. Proc. Natl. Acad. Sci. U.S.A. 111, 5480. https://doi.org/10.1073/pnas.1400668111.

Smith, J., Vance, D., Kemp, R.A., Archer, C., Toms, P., King, M., Zárate, M., 2003. Isotopic constraints on the source of Argentinian loess – with implications for atmospheric circulation and the provenance of Antarctic dust during recent glacial maxima. Earth Planet. Sci. Lett. 212, 181–196. https://doi.org/10.1016/S0012-821X(03)00260-7.

Speer, K.G., Zenk, W., 1993. The flow of Antarctic bottom water into the Brazil basin. J. Phys. Oceanogr. 23, 2667–2682. https://doi.org/10.1175/1520-0485(1993)023<2667:TFOABW>2.0.CO;2.

Spooner, P.T., Thornalley, D.J.R., Ellis, P., 2018. Grain size constraints on glacial circulation in the southwest Atlantic. Paleoceanogr. Paleoclimatol. 33, 21–30. https://doi.org/10.1002/2017PA003232.

Stern, C.R., Frey, F.A., Futa, K., Zartman, R.E., Peng, Z., Kurtis Kyser, T., 1990. Trace-element and Sr, Nd, Pb, and O isotopic composition of Pliocene and Quaternary alkali basalts of the Patagonian Plateau lavas of southernmost South America. Contrib. Mineral. Petrol. 104, 294–308. https://doi.org/10.1007/BF00321486.

Stramma, L., England, M., 1999. On the water masses and mean circulation of the South Atlantic Ocean. J. Geophys. Res.: Oceans 104, 20863–20883. https://doi.org/10.1029/1999JC900139.

Tapani Rämö, O., Heikkilä, P.A., Pulkkinen, A.H., 2016. Geochemistry of Paraná-Etendeka basalts from Misiones, Argentina: some new insights into the petrogenesis of high-Ti continental flood basalts. J. South Am. Earth Sci. 67, 25–39. https://doi.org/10.1016/j.jsames.2016.01.008.

Tingey, R.J., 1991. The regional geology of Archean and Proterozoic rocks in Antractica. In: The Geology of Antarctica. Oxford University Press, pp. 1–73.

Tingey, R.J., Laird, M.J., Barret, P.J., Ford, A.B., Himmelberg, P.F., Barker, P.F., Dalziel, I.W., Storey, B.C., LeMasurier, W.E., Rex, D.C., Anderson, J.B., Bentley, C.R., Denton, G.H., Prentice, M.L., Burckle, L.H., McKelvey, B.C., Cooper, R.A., Shergold, J.H., Thomson, M.R.A., Truswell, E.M., Young, G.C., Colbert, E.H., Behrent, J.C., Rowler, P.D., Williams, P.L., Pride, D.E., Cassidy, W.A., 1991. The Geology of Antarctica. Oxford University Press.

Toggweiler, J.R., Russell, J.L., Carson, S.R., 2006. Midlatitude westerlies, atmospheric CO2, and climate change during the ice ages. Paleoceanography 21. https://doi.org/10.1029/2005PA001154.

Vázquez Riveiros, N., Waelbroeck, C., Skinner, L., Roche, D.M., Duplessy, J.-C., Michel, E., 2010. Response of South Atlantic deep waters to deglacial warming during Terminations V and I. Earth Planet. Sci. Lett. 298, 323–333. https://doi.org/10.1016/j.epsl.2010.08.003.

Waelbroeck, C., Skinner, L.C., Labeyrie, L., Duplessy, J.-C., Michel, E., Vazquez Riveiros, N., Gherardi, J.-M., Dewilde, F., 2011. The timing of deglacial circulation changes in the Atlantic. Paleoceanography 26. https://doi.org/10.1029/2010PA002007.

Waichel, B.L., de Lima, E.F., Viana, A.R., Scherer, C.M., Bueno, G.V., Dutra, G., 2012. Stratigraphy and volcanic facies architecture of the Torres syncline, southern Brazil, and its role in understanding the Paraná–Etendeka continental flood basalt province. J. Volcanol. Geotherm. Res. 215 (216), 74–82. https://doi.org/10.1016/j.jvolgeores.2011.12.004.

Walter, H.J., Hegner, E., Diekmann, B., Kuhn, G., Rutgers van der loeff, M.M., 2000. Provenance and transport of terrigenous sediment in the south Atlantic Ocean and their relations to glacial and interglacial cycles: Nd and Sr isotopic evidence. Geochem. Cosmochim. Acta 64, 3813–3827. https://doi.org/10.1016/S0016-7037(00)00476-2.

Watson, A.J., Bakker, D.C.E., Ridgwell, A.J., Boyd, P.W., Law, C.S., 2000. Effect of iron supply on Southern Ocean CO2 uptake and implications for glacial atmospheric CO2. Nature 407, 730–733. https://doi.org/10.1038/35037561.

Weber, S.L., Drijfhout, S.S., 2007. Stability of the Atlantic Meridional overturning circulation in the last glacial maximum climate. Geophys. Res. Lett. 34 https://doi.org/10.1029/2007GL031437.

Weltje, G.J., 2012. Quantitative models of sediment generation and provenance: state of the art and future developments. Sediment. Geol. 280, 4–20. https://doi.org/10.1016/j.sedgeo.2012.03.010.

Weltje, G.J., Prins, M.A., 2007. Genetically meaningful decomposition of grain-size distributions. Sediment. Geol. 202, 409–424. https://doi.org/10.1016/j.sedgeo.2007.03.007.

Will, T.M., Frimmel, H.E., Zeh, A., Le Roux, P., Schmädicke, E., 2010. Geochemical and isotopic constraints on the tectonic and crustal evolution of the Shackleton Range, East Antarctica, and correlation with other Gondwana crustal segments. Precambrian Res. 180, 85–112. https://doi.org/10.1016/j.precamres.2010.03.005.

Wolff, E.W., Fischer, H., Fundel, F., Ruth, U., Twarloh, B., Littot, G.C., Mulvaney, R., Röthlisberger, R., de Angelis, M., Boutron, C.F., Hansson, M., Jonsell, U., Hutterli, M.A., Lambert, F., Kaufmann, P., Stauffer, B., Stocker, T.F., Steffensen, J.P., Bigler, M., Siggaard-Andersen, M.L., Udisti, R., Becagli, S., Castellano, E., Severi, M., Wagenbach, D., Barbante, C., Gabrielli, P., Gaspari, V., 2006. Southern Ocean sea-ice extent, productivity and iron flux over the past eight glacial cycles. Nature 440, 491–496. https://doi.org/10.1038/nature04614.